The Astrophysical Journal Supplement Series, 217:15 (27pp), 2015 March doi:10.1088/0067-0049/217/1/15

TOMOGRAPHY OF THE *FERMI*-LAT γ-RAY DIFFUSE EXTRAGALACTIC SIGNAL VIA CROSS CORRELATIONS WITH GALAXY CATALOGS

Jun-Qing Xia[1,2], Alessandro Cuoco[3,4,5], Enzo Branchini[6,7,8], and Matteo Viel[9,10]
[1] Key Laboratory of Particle Astrophysics, Institute of High Energy Physics, Chinese Academy of Science, P. O. Box 918-3, Beijing 100049, People's Republic Of China
[2] Collaborative Innovation Center of Modern Astronomy and Space Exploration, People's Republic Of China
[3] Department of Physics, University of Torino, via P. Giuria 1, I-10125 Torino, Italy
[4] Istituto Nazionale di Fisica Nucleare, via P. Giuria 1, I-10125 Torino, Italy
[5] Stockholm University—AlbaNova University Center, Fysikum, SE-10691, Stockholm, Sweden
[6] Dipartimento di Matematica e Fisica, Università degli Studi "Roma Tre," via della Vasca Navale 84, I-00146 Roma, Italy
[7] INFN, Sezione di Roma Tre, via della Vasca Navale 84, I-00146 Roma, Italy
[8] INAF, Osservatorio Astronomico di Roma, Monte Porzio Catone, Italy
[9] INAF Osservatorio Astronomico di Trieste, Via G. B. Tiepolo 11, I-34141, Trieste, Italy
[10] INFN, Sezione di Trieste, via Valerio 2, I-34127, Trieste, Italy
Received 2014 November 13; accepted 2015 January 30; published 2015 March 24

ABSTRACT

Building on our previous cross-correlation analysis (Xia et al. 2011) between the isotropic γ-ray background (IGRB) and different tracers of the large-scale structure of the universe, we update our results using 60 months of data from the Large Area Telescope (LAT) on board the *Fermi Gamma-ray Space Telescope* (*Fermi*). We perform a cross-correlation analysis both in configuration and spherical harmonics space between the IGRB and objects that may trace the astrophysical sources of the IGRB: QSOs in the Sloan Digital Sky Survey (SDSS) DR6, the SDSS DR8 Main Galaxy Sample, luminous red galaxies (LRGs) in the SDSS catalog, infrared-selected galaxies in the Two Micron All Sky Survey (2MASS), and radio galaxies in the NRAO VLA Sky Survey (NVSS). The benefit of correlating the *Fermi*-LAT signal with catalogs of objects at various redshifts is to provide tomographic information on the IGRB, which is crucial in separating the various contributions and clarifying its origin. The main result is that, unlike in our previous analysis, we now observe a significant ($>3.5\sigma$) cross-correlation signal on angular scales smaller than 1° in the NVSS, 2MASS, and QSO cases and, at lower statistical significance ($\sim 3.0\sigma$), with SDSS galaxies. The signal is stronger in two energy bands, $E > 0.5$ GeV and $E > 1$ GeV, but it is also seen at $E > 10$ GeV. No cross-correlation signal is detected between *Fermi* data and the LRGs. These results are robust against the choice of the statistical estimator, estimate of errors, map cleaning procedure, and instrumental effects. Finally, we test the hypothesis that the IGRB observed by *Fermi*-LAT originates from the summed contributions of three types of unresolved extragalactic sources: BL Lacertae objects (BL Lacs), flat spectrum radio quasars (FSRQs), and star-forming galaxies (SFGs). We find that a model in which the IGRB is mainly produced by SFGs ($72^{+23}_{-37}\%$ with 2σ errors), with BL Lacs and FSRQs giving a minor contribution, provides a good fit to the data. We also consider a possible contribution from misaligned active galactic nuclei, and we find that, depending on the details of the model and its uncertainty, they can also provide a substantial contribution, partly degenerate with the SFG one.

Key words: cosmology: observations – cosmology: theory – gamma rays: diffuse background – large-scale structure of universe

1. INTRODUCTION

The origin of the extragalactic γ-ray background (EGB) is still unknown. After its detection and early attempts to unveil its origin (Kraushaar et al. 1972; Fichtel et al. 1973; Mayer-Hasselwander et al. 1982; Padovani et al. 1993; Stecker & Salamon 1996; Sreekumar & Bertsch 1998; Keshet et al. 2004; Strong et al. 2004), major advances have recently been possible thanks to the *Fermi* γ-ray Space Telescope. Observations with the Large Area Telescope (*Fermi*-LAT; Atwood et al. 2009) are resolving an ever growing number of sources, making it possible to characterize their properties, as in, e.g., Ajello et al. (2012, 2014), and to constrain their contribution to the EGB. These constraints are further complemented by comparing the unresolved EGB with semianalytical models of different types of sources, e.g., Stecker & Venters (2011), Makiya et al. (2011), Dobardžić & Prodanović (2014), Tamborra et al. (2014), Ackermann et al. (2012a), and Rephaeli & Persic (2013). Thanks to *Fermi*-LAT a sizable fraction of the EGB is starting to be resolved (Ackermann 2014a). Therefore, to avoid confusion, it is convenient to use a specific term for the unresolved part, which is the quantity we want to study, to distinguish it from the resolved point sources, either masked or subtracted. In the following, we indicate the unresolved component as the isotropic gamma-ray background (IGRB).

The study of the IGRB is hampered by the presence of spurious contributions, like the Galactic foregrounds or bright point sources, that, if not properly subtracted, contaminate the mean signal and generate systematic errors in the analysis of the true signal. These systematic uncertainties can, in principle, be mitigated by considering the angular correlation properties of the IGRB (Ackermann 2012a). In practice, however, the autocorrelation signal is also quite prone to the aforementioned systematics, which, being not perfectly isotropic, affect the measurements on various angular scales. Instead, an effective way to enhance the signal and filter out systematic effects is to cross correlate the IGRB with several different distributions of extragalactic objects that may or may not trace the actual

source of the IGRB but certainly do not correlate with the sources of systematic errors. This approach has been proposed and adopted by, e.g., Cuoco et al. (2008), Ando & Pavlidou (2009), and Xia et al. (2011). Besides the cross correlation with catalogs of extragalactic objects, a further possibility recently proposed is to cross correlate the IGRB with weak gravitational lensing maps (Camera et al. 2013, 2014; Fornengo et al. 2014; Fornengo & Regis 2014; Shirasaki et al. 2014), which presents the advantage of tracing the gravitational potential without any bias. Furthermore, it has been recently shown that cross correlation of the IGRB with galaxy catalogs can provide tight constraints on the dark matter annihilation (Ando 2014).

Results so far have been negative because no clear correlation signal has been detected with a large statistical significance. For example, in Xia et al. (2011) the significance of the correlation between *Fermi* data and Sloan Digital Sky Survey (SDSS) luminous red galaxies (LRGs) was reported to be only at the 2σ confidence level.

Nevertheless, these results have been used to set upper limits on the contribution of different types of potential γ-ray sources such as blazars and star-forming galaxies (SFGs) as well as on the mass and cross section of weakly interacting massive particle (WIMP) dark matter candidates that may also contribute to the γ-ray background through their self-annihilation (e.g., Ando & Komatsu 2013; Cholis et al. 2014).

The goal of this work is to extend and improve on the original study of Xia et al. (2011) using the most recent γ-ray maps obtained with the *Fermi*-LAT. We estimate the two-point angular cross-correlation function (CCF) and the cross-angular power spectrum (CAPS) of the *Fermi*-LAT IGRB with a variety of catalogs of objects: SDSS DR6 quasars (Richards et al. 2009), SDSS DR8 LRGs (Abdalla et al. 2008), NRAO VLA Sky Survey (NVSS) radio galaxies (Blake & Wall 2002), Two Micron All Sky Survey (2MASS) galaxies (Jarrett 2000), and DR8 SDSS main sample galaxies (Aihara et al. 2011). These catalogs have in common (1) a large sky coverage that could allow maximizing a potential cross-correlation signal and (2) the fact that they have already been used to perform quantitative cosmological studies of the large-scale structures (LSS). The fact that they contain different types of sources that span different ranges of redshifts is important because it increases the sensitivity of the cross-correlation analysis to (1) the type of sources that contribute to the IGRB and (2) the cosmic epoch in which this contribution has been provided.

In Xia et al. (2011) we predicted that after 10 years of data taking by the *Fermi*-LAT we would be able to detect a possible contribution to the γ-ray background from relatively nearby ($z \leqslant 2$) sources with a confidence level of ~97%. This prediction was quite conservative becase it was based on the expected Poisson noise level. Improvements (1) in the model for the Galactic diffuse signal and (2) in the characterization of the instrumental point-spread function (PSF) that allows pushing the analysis to energies lower than 1 GeV and to scales smaller than 1°, and finally, (3) the increase in the number of resolved sources allow us to improve our conservative estimate and justify our decision to repeat the cross-correlation analysis using the five-year *Fermi* maps with energies as small as 0.5 GeV.

Following Xia et al. (2011), we compare the results of the cross-correlation analysis with theoretical predictions obtained under the hypothesis that the diffuse γ-ray background has contributions from known extragalactic sources and set constraints on popular candidates like galaxies with strong star-formation activity and two types of blazars: the flat spectrum radio quasars (FSRQ) and the BL Lacertae (BL Lac) objects.

In this work we assume a flat cold dark matter model with a cosmological constant (ΛCDM) with cosmological parameters $\Omega_b h^2 = 0.0222$, $\Omega_c h^2 = 0.1189$, $\tau = 0.095$, $h = 0.678$, $\ln 10^{10} A_s = 3.097$ at $k_0 = 0.05$ Mpc^{-1}, and $n_s = 0.961$ that are in agreement with recent *Planck* results (Planck collaboration et al. 2013a).

The layout of this paper is as follows. In Section 2 we briefly review the theoretical background of the cross-correlation analysis. In Section 3 we present the *Fermi* maps and the various masks and discuss the procedure adopted to eliminate the potential spurious contributions to the extragalactic signal. The maps of the angular distribution of the extragalactic objects that we cross correlate with the *Fermi* maps are presented in Section 4. In Section 5 we describe the statistical estimators used in our cross-correlation analysis, and in Section 6 we test the robustness of the results to the cleaning procedure and to the instrument response modeling and to the data selection. The results are presented in Section 7, compared to model predictions in Section 8, and discussed in Section 9, in which we also summarize our main conclusions.

2. THEORETICAL BACKGROUND

Here we briefly summarize the theoretical framework adopted in our analysis. In this work we use the same formalism as in Xia et al. (2011), to which we refer the reader for a more thorough discussion.

Let us consider a population of γ-ray sources, j, with power-law energy spectra $I(E) \propto E^{1-\Gamma_j}$ characterized by a luminosity function (LF) $\Phi_j(L_\gamma, \Gamma, E, z)$ in which we highlight the explicit dependence on the observed γ-ray energy E, the rest-frame luminosity of the sources L_γ (generally expressed in erg s^{-1}), cosmological redshift z, and photon index $\Gamma_j > 1$. The contribution of this population to the differential *energy* flux is

$$\frac{dI_j}{dE} = \frac{c}{4\pi} \int \Big[\int_{L_{\rm MIN}}^{L_{\rm MAX}(z)} \int_{\Gamma_m}^{\Gamma_M} \Phi_j\big(L_\gamma, \Gamma, (1+z)E, z\big)\Big) \times L_\gamma dL_\gamma d\Gamma \Big] \frac{dz}{(1+z)H(z)}, \quad (1)$$

where $H(z) = H_0[(1+z)^3\Omega_M + \Omega_\Lambda]$ represents the expansion history in the assumed cosmological model and $(1+z)$ accounts for the cosmological redshift. All sources along the line of sight contribute to the integral over z.

The integration over L_γ is performed within a finite luminosity range. We set the upper value equal to

$$L_{\rm MAX}(z) = 4\pi d_L^2(z) S_{\rm lim} (1+z)^{-2+\Gamma_j}, \quad (2)$$

where d_L is the luminosity distance in the adopted cosmology and $S_{\rm lim}$ is the (energy) flux detection limit. In general, the flux detection threshold depends on the power-law index. This dependence is strong for the photon flux and much weaker for the energy flux. For this reason, in this work we shall ignore the correlation between $S_{\rm lim}$ and Γ_j. This implies that resolved sources are excluded and that the integral (Equation (1)) has contributions only from unresolved sources. The lower integration limit, $L_{\rm MIN}$, is taken from recent literature for

specific source classes, as we shall discuss in the next section. We note that the integral converges and setting $L_{\rm MIN}$ to much smaller values has very little effect on the final results; that is, our results are robust against the value of $L_{\rm MIN}$. The choice of $S_{\rm lim}$ depends on the γ-ray source catalog used to mask resolved point sources. In the following we will use the 2FGL (Nolan et al. 2012) source catalog and a preliminary version of the 3FGL (Acero & Ackermann 2015) catalog. Typical values of the source-detection thresholds (in units of integrated energy flux above 100 MeV) are 5×10^{-12} erg cm^{-2}s^{-1} and 2.5×10^{-12} erg cm^{-2}s^{-1}, respectively, for the 2FGL and 3FGL catalog (Acero & Ackermann 2015), with the lower threshold of the 3FGL catalog in part due to the larger data set used (four years versus two years) and in part to the improved characterization of the response of the LAT. In practice, however, the luminosity density $\rho_\gamma(z)$ that we shall use to characterize the contribution of a given type of sources to the energy flux is weakly dependent on the detection threshold; that is, similar results are obtained with the 3FGL and 2FGL thresholds, even if the former has a deeper reach in flux than the latter. This reflects the fact that below 100 GeV the bulk of the EGB is still unresolved in both the 2FGL and 3FGL catalogs. For this same reason, the energy density is insensitive to the precise modeling of the detection efficiency, which is not exactly a step function but represents rather a smooth transition in flux between zero and full efficiency.

In the integration over Γ we assume that the intrinsic distribution of photon indices is a Gaussian, which implies that for a given redshift z and luminosity L_γ the LF has the form

$$\Phi\left(L_\gamma, z, \Gamma\right) \propto e^{-\frac{\left(\Gamma-\mu\left(L_\gamma\right)\right)^2}{2\sigma^2}}, \quad (3)$$

where μ and σ are, respectively, the mean and dispersion of the distribution. The mean is allowed to be a function of the source luminosity (expressed in units of 10^{48} erg s^{-1}):

$$\mu\left(L_\gamma\right) = \mu^* + \beta\times\left(\log_{10}\left(L_\gamma\right) - 46\right). \quad (4)$$

Because in the luminosity range of interest $\sigma \ll \mu$, as we will see, then we can approximate the Γ distribution with a Dirac delta centered on $\Gamma = \mu$. With this approximation the integrated flux I_j(>E) can be expressed as

$$I_j(>E) \equiv \int_E^\infty \frac{dI_j}{dE}dE = \frac{cE^{2-\Gamma_j}}{4\pi}\int\rho_\gamma(z)dz, \quad (5)$$

where

$$\rho_\gamma(z) \equiv \int_{L_{\rm MIN}}^{L_{\rm MAX}(z)} \Phi_j\left(L_\gamma, z\right)L_\gamma\frac{(1+z)^{-\mu_j\left(L_\gamma\right)}}{H(z)}dL_\gamma \quad (6)$$

is the the mean luminosity density at z and $\Phi_j(L_\gamma, z) \equiv \Phi_j(L_\gamma, z, \Gamma = \mu(L_\gamma))$. In this paper we deal with maps of photon counts rather than energy flux, the photon flux (above energy E) being simply $(2-\Gamma_j)/(1-\Gamma_j)\times I_j(>E)/E$. We will consider maps of integrated flux above three energy thresholds: $I(>E = 0.5\ {\rm GeV})$, $I(>E = 1\ {\rm GeV})$, and $I(>E = 10\ {\rm GeV})$.

Variations in the number density of unresolved sources, $n_\gamma(z, \boldsymbol{x})$, are responsible for the local fluctuation in the γ-ray luminosity density, $\rho_\gamma(z, \boldsymbol{x})$, and, therefore, in the integrated γ-ray flux. If the luminosity is proportional to the number of sources, then the two fluctuations in n_γ and ρ_γ are related through

$$\delta_\gamma(z, \boldsymbol{x}) \equiv \frac{\rho_\gamma(z, \boldsymbol{x}) - \rho_\gamma(z)}{\rho_\gamma(z)} = \frac{n_\gamma(z, \boldsymbol{x}) - n_\gamma(z)}{n_\gamma(z)} \equiv \delta_{n_\gamma}(z, \boldsymbol{x}), \quad (7)$$

where the mean number density of sources is $n_\gamma \equiv \int\Phi(L)dL$. We further assume a linear mapping, called biasing, between mass density ρ_m and the number density of objects:

$$\delta_{n_\gamma}(z, \boldsymbol{x}) \equiv b_\gamma(z)\delta_m(z, \boldsymbol{x}) = b_\gamma(z)\frac{\rho_m(z, \boldsymbol{x}) - \rho_m(z)}{\rho_m(z)}, \quad (8)$$

where we allow for a redshift-dependent bias parameter, $b_\gamma(z)$.

Fluctuations in the integrated flux along the generic direction $\boldsymbol{n}$ can be obtained from (5) and the linear biasing prescription (8):

$$\delta I(\boldsymbol{n}) \equiv \frac{I(>E, \boldsymbol{n}) - I(>E)}{I(>E)} = \frac{\int\rho_\gamma(z)b_\gamma(z)\delta_m(z, \boldsymbol{x})dz}{I(>E)}, \quad (9)$$

where $I \equiv I(>E)$ indicates the γ-ray mean flux and $I(\boldsymbol{n}) \equiv I(>E, \boldsymbol{n})$ is the energy flux along the generic direction $\boldsymbol{n}$.

Our goal is to investigate the cross correlation between the diffuse IGRB maps and the sky-projected spatial distribution of different types of extragalactic objects. The angular cross-power spectrum between the extragalactic background $I(>E, \boldsymbol{n})$ and the fluctuation of discrete sources, j, can be expressed as

$$C_l^{I,j} = \frac{2}{\pi}\int k^2P(k)\left[G_l^I(k)\right]\left[G_l^j(k)\right]dk, \quad (10)$$

where $P(k)$ is the power spectrum of density fluctuations, l is the multipole of the spherical harmonics expansion, and the functions $G(k)$ specify the contribution of each field to the cross-correlation signal. More specifically, the contribution of the IGRB is given by

$$G_l^I(k) = \int\rho_\gamma(z)b_\gamma(z)D(z)j_l[k\chi(z)]dz \quad (11)$$

where $j_l[k\chi(z)]$ are spherical Bessel functions, $D(z)$ is the linear growth factor of density fluctuations, and $\chi(z)$ is the comoving distance to redshift z. The analogous quantity for the number density fluctuations in a population of discrete objects is

$$G_l^j(k) = \int\frac{dN(z)}{dz}b_j(z)D(z)j_l[k\chi(z)]dz, \quad (12)$$

where $dN(z)/dz$ is the redshift distribution of the objects. Here we make the hypothesis that these objects, which do not necessarily coincide with the sources of the IGRB, also trace the underlying mass density field modulo some z-dependent linear bias parameter $b_j(z)$.

Note that in the cross correlation we consider the integrated flux $I(>E, \boldsymbol{n})$ rather than its dimensionless analog $\delta I(\boldsymbol{n})$ given in Equation (9). With this choice, the cross-correlation signal is

Table 1
Parameters of the LDDE LFs Taken from Ajello et al. (2012) for FSRQs and Ajello et al. (2014) for BL Lacs

Model	A^{a}	γ_1	$L_*{}^{b}$	γ_2	z_c^*	p_1^*	τ	p_2	α	μ^*	β	σ
BLLacs1 LDDE	3.39×10^4	0.27	0.28	1.86	1.34	2.24	4.92	−7.37	4.53×10^{-2}	2.10	6.46×10^{-2}	0.26
BLLacs2 LDDE	9.20×10^2	1.12	2.43	3.71	1.67	4.50	0.0	−12.88	4.46×10^{-2}	2.12	6.04×10^{-2}	0.26
FSRQ LDDE	3.06×10^4	0.21	0.84	1.58	1.47	7.35	0.0	−6.51	0.21	2.44	0.0	0.18

[a] In units of 10^{-13} Mpc^{-3} erg^{-1} s.
[b] In units of 10^{48} erg s^{-1}.

robust to any spurious monopole term arising from an incorrect subtraction of the model Galactic diffuse signal or charged particle contamination. One implication of this choice is that our model cross-correlation signal (10) is dependent on the mean integrated flux, $I(>E)$. For this reason, and to account for uncertainties in the estimate of the mean IGRB signal, we allow for some freedom in the normalization of the LF of the putative γ-ray sources and, accordingly, add an additional free parameter in the model.

In this work we also estimate the angular two-point CCF of the flux maps and discrete object catalogs, which is simply the Legendre transform of the angular power spectrum

$$\left\langle I\left(>E, \boldsymbol{n_1}\right)\delta_j(\boldsymbol{n_2})\right\rangle = \sum_l \frac{2\,l+1}{4\pi} C_l^{I,j} P_l[\cos(\theta)], \quad (13)$$

where $P_l[x]$ are the Legendre polynomials and θ is the separation angle between directions $\boldsymbol{n_1}$ and $\boldsymbol{n_2}$. The angular two-point correlation function and power spectrum are two ways of expressing the same information. However, in practice, the two statistics are somewhat complementary because they probe different scales with different efficiency and their respective estimators are prone to different types of biases. For this reason we shall compute both quantities.

2.1. Modeling the Mean Flux and the Cross-correlation Signal

One of the aims of this work is to compare the measured cross-correlation signal with model predictions obtained under the assumption that some specific type of unresolved sources contributes to the IGRB. We note that even autocorrelation studies can provide constraints on the nature and spatial clustering of the sources contributing to the signal (e.g., Persic et al. 1989). In our case, we are required to model (1) the correlation properties of the underlying mass density field; (2) its relation with discrete tracers, i.e., the biasing prescription; and (3) the mean IGRB flux. To model the cross-correlation signal, we consider the cosmologically evolving mass density power spectrum, $P(k,z)$, obtained from the public code `CAMB` (Lewis et al. 2000) for the linear part and the `Halofit` built-in routine for nonlinear evolution (Smith et al. 2003). In addition, we use the linear growth factor $D(z)$ and the comoving distance $\chi(z)$ appropriate for the cosmological model adopted.

To model the bias and the mean IGRB signal, we need to select a class of objects that are likely to contribute to the IGRB and specify the energy spectrum, LF, and fraction of IGRB contributed by the source, f_j. Here we consider three different candidates: FSRQs, BL Lacs, and SFGs.

1. FSRQs are a type of AGN (blazars) with a relativistic jet pointing close to the line of sight. Ajello et al. (2012) recently determined the γ-ray LF of these objects, which they have parameterized in the framework of a luminosity-dependent density evolution (LDDE) model:

$$\Phi\left(L_\gamma, z=0, \Gamma\right) = \frac{A}{\ln(10)L_\gamma}\left[\left(\frac{L_\gamma}{L_*}\right)^{\gamma_1} + \left(\frac{L_\gamma}{L_*}\right)^{\gamma 2}\right]^{-1} \times e^{-\frac{\left(\Gamma-\mu\left(L_\gamma\right)\right)^2}{2\sigma^2}}. \quad (14)$$

The term in parentheses, a smoothly joined double power-law function, represents the LF of the local FSRQs, and the exponential term is the same photon index distribution as Equation (3). In the LDDE model, the LF at the redshift z can be expressed as

$$\Phi\left(L_\gamma, z, \Gamma\right) = \Phi\left(L_\gamma, z=0, \Gamma\right) \times e\left(z, L_\gamma\right), \quad (15)$$

where

$$e\left(z, L_\gamma\right) = \left[\left(\frac{1+z}{1+z_c\left(L_\gamma\right)}\right)^{-p_1\left(L_\gamma\right)} + \left(\frac{1+z}{1+z_c\left(L_\gamma\right)}\right)^{-p_2}\right]^{-1} \quad (16)$$

with

$$p_1\left(L_\gamma\right) = p_1^* + \tau \times \left(\log_{10}\left(L_\gamma\right) - 46\right) \quad (17)$$

and

$$z_c\left(L_\gamma\right) = z_c^* \cdot \left(L_\gamma/10^{48}\right)^{\alpha}. \quad (18)$$

Here, z_c represents the luminosity-dependent redshift at which the evolution changes from positive to negative, and z_c^* is the evolutionary peak for an object with a luminosity of 10^{48} erg s^{-1}. This LDDE LF model is specified by the 12 parameters listed in Table 1 with the particular values determined by Ajello et al. (2012) by fitting γ-ray data. In the fit, the authors have set $\beta = \tau = 0$: they have assumed that neither the overall shape of the LF nor the spectral index depend on the luminosity of the sources, L_γ. Note that the evolutionary term $e(z,L_\gamma)$ in Equation (16) is not equal to unity at $z = 0$. To derive the density $\rho_\gamma(z)$ in Equation (6) required to calculate the correlations, we set $L_{\rm MIN} = 10^{44}$ erg s^{-1} as recommended in Ajello et al. (2012), although, as already explained, choosing a lower value or even zero does not significantly affect the results.

The parameters of the LF uniquely determine the contribution of FSRQs to the mean diffuse IGRB signal. However, as anticipated, in this work we prefer to keep

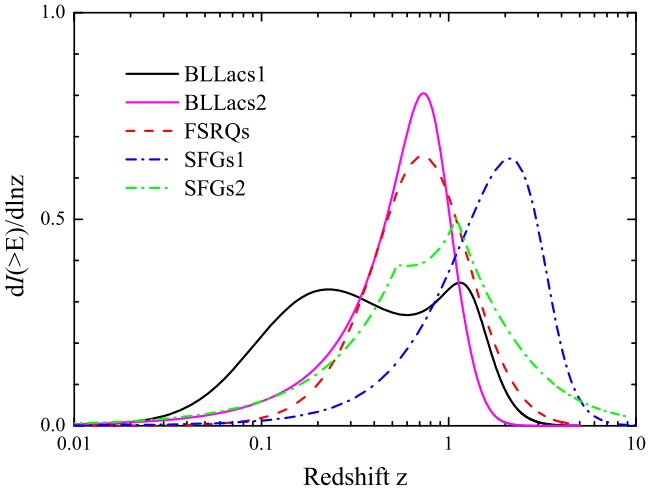

Figure 1. Integrated γ-ray flux per logarithmic redshift bin $dI\,(>E)/d\,\ln z$ as a function of z for three different source classes: FSRQs (red, dashed), BL Lacs (black or magenta, continuous), and star-forming galaxies (blue or green, dot-dashed).

the normalization of the LF free. This additional degree of freedom is meant to absorb experimental errors in the measurement of the mean diffuse IGRB signal and uncertainties in modeling the clustering of the sources. The resulting redshift distribution of the γ-ray flux contributed by FSRQs shown in Figure 1 is rather broad and peaks at $z \sim 0.5$.

The last ingredient of the model is the bias of the sources. Here we adopt the redshift-dependent AGN bias proposed by Bonoli et al. (2009) in the framework of the semianalytic models of AGN–black hole coevolution: $b_{\rm FSRQ}(z) = 0.42 + 0.04(1+z) + 0.25(1+z)^2$. To test the robustness of our results to the biasing scheme, we have considered two alternative bias models: (1) the rather unphysical case of a constant bias $b_{\rm FSRQ} = 1.04$, obtained by considering it equal to the bias model of Bonoli et al. (2009) estimated at $z = 0.5$; and (2) a linear, z-dependent model in which the bias is set equal to that of a $10^{13}\,M_\odot$ halo. This latter choice reproduces the bias of X-ray-selected AGNs estimated by Koutoulidis et al. (2013) and represents an upper limit because the bias of optically selected AGNs is matched by the bias of $10^{13}\,M_\odot$ halos.

2. BL Lacs. These sources represent a different subclass of blazars with, on average, lower luminosities than FSRQs. To model their LF, we adopt the LDDE functional form as in Equation (14) and set the free parameters according to the best fit to the γ-ray data obtained by Ajello et al. (2014). We consider two possibilities corresponding to the two sets of parameters in Table 1. In the first case, which we dub BLLacs1, the authors let all parameters freely vary. In the model BLLacs2, they instead set $\tau = 0$, basically switching off the dependence on the luminosity of the p_1 index in the evolutionary term. It should be stressed that the BLLacs1 model represents a better fit to the data in Ajello et al. (2014). Nonetheless, we also consider model BLLacs2 to study the robustness of the interpretation of the cross correlation in terms of BL Lacs. In accordance with Ajello et al. (2014), we set $L_{\rm MIN} = 7 \times 10^{43}$ erg s^{-1} for the calculation of the $\rho_\gamma(z)$ integral.

The redshift distribution of the γ-ray flux of BL Lacs for the two models considered is shown in Figure 1. In both cases the distribution is rather broad. However, in BLLacs1 the distribution is more local and peaks at $z \sim 0.1$, whereas in BLLacs2 the peak is at much higher redshift ($z \sim 0.7$), although with a significant tail at low z. We assume that the biasing of BL Lacs is the same in both models and equal to that of FSRQs, i.e., $b_{\rm BLLac} = b_{\rm FSRQ}$. The robustness of the results on this choice is also tested using the same alternative bias models considered for FSRQs.

3. SFGs. As reference and comparison with our previous work (Xia et al. 2011), we adopt the phenomenological model of Fields et al. (2010) in which the γ-ray emission in SFGs over cosmic time is proportional to their star-formation rate and the gas mass fraction, both normalized to the present values in the Milky Way (MW). The energy spectrum is assumed to be similar to the one observed in the MW, which can be modeled approximately as a broken power law with photon indexes $\Gamma \sim 1.5$ and $\Gamma \sim 2.475$ above and below $\sim$500 MeV, respectively. The contribution to the IGRB, shown in Figure 1, is spread over a wide redshift range and peaks at $z \sim 1$, with a high-redshift tail more extended than that of BL Lacs and FSRQs. We dub this model SFGs1.

For the sake of completeness, we consider also a second model (SFGs2), originally proposed by Ackermann et al. (2012a) and recently revised by Tamborra et al. (2014). The ingredients of this model are the SFG LF obtained from infrared observations (Rodighiero et al. 2010; Gruppioni et al. 2013) and the empirical relation between luminosity in the infrared and γ-ray bands calibrated using samples of local galaxies observed in both bands and assumed to be valid at all redshifts (Ackermann et al. 2012a). The most recent IR observations of Gruppioni et al. (2013) have enabled the measurement of the LFs of different subpopulations of galaxies. Specifically, Gruppioni et al. (2013) subdivide the infrared galaxies into normal spiral galaxies (SP), starburst galaxies (SB), and galaxies hosting an AGN but whose infrared emission is still dominated by star-forming activity (SF-AGN) and provide the LFs separately for each subpopulation. We model the γ-ray emission separately for the three populations by assuming a power-law energy spectrum with $\Gamma = 2.475$ for SP and SF-AGN and of $\Gamma = 2.2$ for SB (Ackermann et al. 2012a). To test whether the redshift distribution of the γ-ray emission is robust with respect to the assumed spectral shape of galaxies, we use the LF of the whole population of infrared objects from Gruppioni et al. (2013). Assuming a single global index $\Gamma = 2.475$ for this population does not significantly modify the results. It has to be noted that in addition to the contribution from SP, SB, and SF-AGN, this global LF also contains a contribution from pure AGNs, which is, however, very subdominant. The IGRB contribution of SP + SB + SF-AGN as a function of redshift is plotted in Figure 1. The distribution is significantly different than in model SFGs1 because in this case the IGRB is mostly

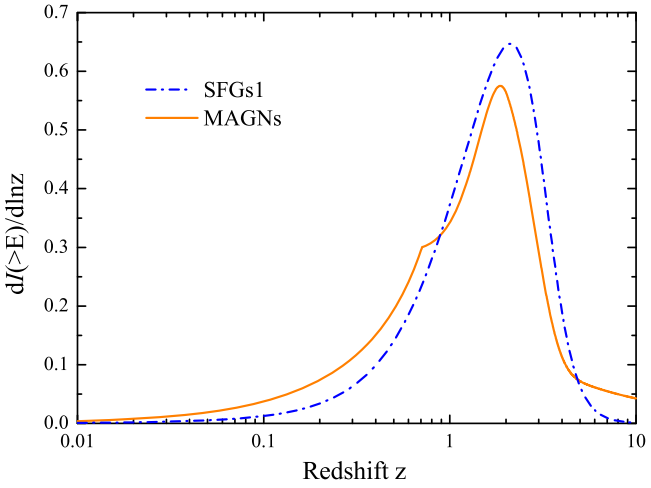

Figure 2. Comparison between the γ-ray flux per logarithmic redshift bin $dI\,(>E)/d\,\ln z$.

contributed by low-redshift galaxies. The discrepancy between the two distributions reflects a fundamental difference between the two models. Both models use the luminosity density in the infrared band, in Fields et al. (2010) assuming that it is a good tracer of the star-formation history (which is a common assumption; see, for example, the discussion in Rodighiero et al. 2010), and in Ackermann et al. (2012a) assuming that it is a tracer of the γ-ray LF itself. However, model SFGs1 further contemplates the possibility of a time-dependent gas quenching that reduces the γ-ray emission at low redshift. As a result, we expect that the two models predict very different cross-correlation signals, despite having similar γ-ray luminosities integrated over redshift (Tamborra et al. 2014).

Finally, based on the observations in Afshordi et al. (2004) and theoretical arguments (Wilman et al. 2008), we assume for both models that SFGs trace the underlying mass density field with no bias (i.e., $b_{\rm SFG} = 1$). We also consider an alternative case in which the bias of the SFGs is set equal to that of a MW-sized halo of $10^{12}\,M_{\odot}$.

2.2. Misaligned AGNs

Another type of source that potentially contributes to the IGRB is misaligned active galactic nuclei (MAGNs; di Mauro et al. 2014; Inoue 2011). Similarly to the case of SFGs, too few MAGNs have been detected in γ-rays to determine their LF directly in this band. Instead, the γ-ray LF is inferred from that measured in some other band by exploiting the observed relation between the luminosities in the two bands. For MAGNs this is done by considering the radio band, i.e., by using the observed MAGN radio LF and the radio-to-γ luminosity relation. The latter relation is calibrated on a local sample of objects for which observations in both bands are available and then extrapolated at all redshifts.

We did follow this procedure and used both the radio LF of Willott et al. (2001) and the radio –γ-ray luminosity relation derived in di Mauro et al. (2014) to obtain the MAGN contribution to the IGRB at all redshifts. The result is shown in Figure 2, which is analogous to Figure 1 but featuring only the MAGN and the SFGs1 models. The main point here is the similarity between the two distributions that peak at $z \sim 2$ and extend to much higher redshift. We also note that while the SFG distribution is smooth, the MAGN exhibits a feature at $z \sim 1$. This reflects the composite nature of the radio-band LF that receives contributions from different types of objects with sharp breaks in their redshift distributions.

For the scope of our analysis, the fact that the two redshift distributions are similar implies a potential degeneracy in the model predictions. This degeneracy can be broken only if the linear bias parameters of the two populations, upon which the amplitude of the clustering depends, are different. In fact, we do expect that the bias of the MAGNs, which are typically associated with massive dark matter halos, is higher than that of the SFGs1, and, as a consequence, the MAGN bias is higher than that of SFGs at all redshifts (see, e.g., Wilman et al. 2008; Lindsay et al. 2014 and references therein). This and the fact that the bias is an increasing function of redshift and that both populations contribute to the IGRB out to high redshifts make it possible, in principle, to discriminate between the two populations through a cross-correlation analysis. In practice, however, the bias of both populations is ill-constrained by present observations.

For this reason, in the present analysis, we focus on those objects for which the contribution to the IGRB and its anisotropy are more robust to the uncertainties in the bias. In fact, we have considered blazars, because their $dI\,(>E)/d\,\ln z$ is suppressed at high redshift where the bias of the objects is expected to increase, and SFG, because their bias is expected to be close to unity even at high redshifts. For the very same reason, we have decided not to include MAGN in our model: they can be found at very high redshift, and their bias is large and rapidly increases with redshift. Of course this does not mean that MAGNs do not contribute to the correlation signal, only that our analysis will not be able to discriminate between SFG and MAGN contributions. Therefore it should be kept in mind that the SFG contribution, which we will study in the following, may actually include an MAGN signal as well and that our model cross-correlation signal, entirely based on blazars and SFGs, could be underestimated at high redshifts.

2.3. Further Theoretical Contributions

All of our models assume that the discrete sources sample, according to a deterministic bias relation, the underlying mass density field whose two-point clustering properties can be quantified by a nonlinear power spectrum that can be obtained using `CAMB` + `Halofit`. This is an approximation that ignores the presence of substructures within virialized halos and, consequently, underestimates the power on small scales. In the language of the halo model (Cooray & Sheth 2002), we underestimate the *one-halo* term contribution to the correlation signal. Theoretical modeling of this term is challenging because it depends on several characteristics, both of the catalog and of the γ-ray emitting population, that are quite uncertain. For example, it is necessary to specify how the galaxies of a catalog are distributed on average within a DM halo of given mass and, analogously, how γ-ray sources of different luminosities populate the same DM halo. Both quantities can be modeled, but within large uncertainties. Further details are discussed, for example, in Ando (2014), Camera et al. (2014), and Ando et al. (2007). On the contrary, the shape of the *one-halo* term is easier to model. Assuming point-like DM halos, this term would simply be a constant in multipole space or a delta-like

term at $\theta = 0^\circ$ in the CCF. Small distortions from a constant arise considering the finite extent of DM halos and are typically important at very high multipoles ($\gtrsim$1,000) for halos at low redshift ($\lesssim$0.1). In the following, we will thus adopt a phenomenological approach and model this term as constant in ℓ with a free normalization and check against the data whether there is a preference for the inclusion of a *one-halo* correlation.

A second assumption of our model is that the sources responsible for the γ-ray signal and the various astrophysical sources that we cross correlate trace the same mass density with different bias relations: that is, they are not the same population. There is, however, the possibility that they are the same population seen at two different wavelengths (or two populations that largely overlap each other). In this case one would expect a strong cross-correlation peak in the CCF at $\theta = 0^\circ$, corresponding, again, to a constant in multipole space. With enough angular resolution, this possibility could be distinguished, in principle, from a pure *one-halo* term, due to the distortion induced by the finite extent of the DM halo in the latter (with the possible caveat of a positive correlation signal at $\theta \gtrsim 0^\circ$ that may arise even in this case when the emission in two different bands originates from two separate regions of the same object, like, for example, possibly in the case of the nucleus and the jet of an AGN). Typically, however, the LAT PSF is too large to allow discrimination between the two cases. We will thus model both terms as constant in multipole space and consider their sum as a single contribution whose presence will be tested in the data. We will indicate these contributions collectively as *one-halo*-like terms.

3. *FERMI*-LAT MAPS

In this section we describe the IGRB maps obtained from five years of *Fermi*-LAT data taking and the masks and templates used to subtract contributions from (1) γ-ray resolved sources, (2) Galactic diffuse emission due to interactions of cosmic rays with the interstellar medium, and (3) additional Galactic emission located at high Galactic latitude in prominent structures such as the *Fermi* Bubbles (Su et al. 2010; Ackermann 2014c) and Loop I (Casandjian & Grenier 2009). The validity of the masking procedure, its effectiveness in removing foreground and resolved source contributions to the IGRB signal, and its impact on cross-correlation analysis are assessed in Section 6.

Fermi-LAT is the primary instrument on board the *Fermi* Gamma-ray Space Telescope launched in 2008 June (Atwood et al. 2009). It is a pair-conversion telescope covering the energy range between 20 MeV and >300 GeV. Because of its excellent angular resolution ($\sim$0.°1 above 10 GeV), very large field of view ($\sim$2.4 sr), and very efficient rejection of background from charged particles, it is the best experiment to investigate the nature of the IGRB in the gigaelectronvolt energy range.

For our analysis, we used 60 months of data from 2008 August 4 to 2013 August 4. More specifically, we used the `P7REP_CLEAN` event selection[11] in order to ensure a low level of cosmic-ray (CR) background contamination. Further, to greatly reduce the contamination from the bright Earth limb emission, we exclude photons detected (1) with measured zenith angle larger than 100° or (2) when the rocking angle of the LAT with respect to the zenith was larger than 52°. In order to generate the final flux maps, we have produced the corresponding exposure maps using the standard routines from the LAT *Science Tools*[12] version 09-32-05, using the latest recommended `P7REP_CLEAN_V15` instrument response functions (IRFs). We use both back-converting and front-converting events, and we checked the robustness of the results using either data subsample (see Section 6.3). The GaRDiAn package (Ackermann 2012b, 2009) was then used to pixelize both photon count and exposure maps in HEALPix[13] format (Górski et al. 2005). The maps contain $N_{\rm pix} = 3{,}145{,}728$ pixels with an angular size of $\sim 0.^\circ 11 \times 0.^\circ 11$ corresponding to the HEALPix resolution parameter $N_{\rm side} = 512$. Finally, the flux maps are obtained by dividing the count maps by exposure maps in three energy ranges: $E > 500$ MeV, $E > 1$ GeV, and $E > 10$ GeV.

To reduce the impact of the Galactic emission on our analysis focused on the IGRB, we apply a Galactic latitude cut $|b| > 30^\circ$ in order to mask the bright emission along the Galactic plane. Moreover, we also exclude the region associated with the *Fermi* Bubbles and the Loop I structure. In Xia et al. (2011) we experimented with different latitude cuts and found that $|b| > 30^\circ$ represents the best compromise between pixel statistics and Galactic contamination. The corresponding mask, obtained from the tabulated contours of the *Fermi* Bubbles given in Su et al. (2010), is shown in the bottom panel of Figure 4 as the bulge-like central region, with the horizontal strip mask corresponding to the latitude cut. The mask also features a number of smaller holes placed at the positions of all resolved sources in a preliminary version of the 3FGL catalog. In the $E > 1$ GeV maps, all sources are masked out with a disk of 1° radius. For $E > 0.5$ GeV we used larger disks of 2° but only for the 500 sources with the highest integrated flux above 100 MeV in the catalog, while the remaining ones are still masked with disks of 1°. Finally, to exclude the contribution from the Small and Large Magellanic Clouds, which are more extended, we used two larger circles with 3° radius. To test the robustness of our results on the subtraction of resolved sources, we also built a similar mask using the previous 2FGL catalog (`gll_psc_v08.fit`[14]). Further details are given in Section 6.2. When cross correlating with a given galaxy catalog, the mask specific to that catalog is further employed. The masks for the catalogs we use can be seen in Xia et al. (2011).

Although we select a part of the sky at high Galactic latitude, the Galactic diffuse emission in this region is still significant and needs to be removed. For this purpose, and to check the robustness to this correction, we use two models of Galactic diffuse emission: `ring_2year_P76_v0.fits`[15] and `gll_iem_v05_rev1.fit`, which we subtract from the observed emission to obtain the *cleaned* maps. Both models are based on a fit of the LAT data to templates of the H I and CO gas distribution in the Galaxy as well as on an inverse Compton model obtained with the GALPROP code.[16] The first model

[11] See http://www.slac.stanford.edu/exp/glast/groups/canda/lat_Performance.htm for a definition of the `P7REP` and `P7` event selections and their characteristics.

[12] http://fermi.gsfc.nasa.gov/ssc/data/analysis/documentation/Cicerone/

[13] http://healpix.jpl.nasa.gov/

[14] http://fermi.gsfc.nasa.gov/ssc/data/access/lat/2yr_catalog/

[15] http://fermi.gsfc.nasa.gov/ssc/data/access/lat/BackgroundModels.html

[16] A more detailed description can be found at http://fermi.gsfc.nasa.gov/ssc/data/access/lat/BackgroundModels.html

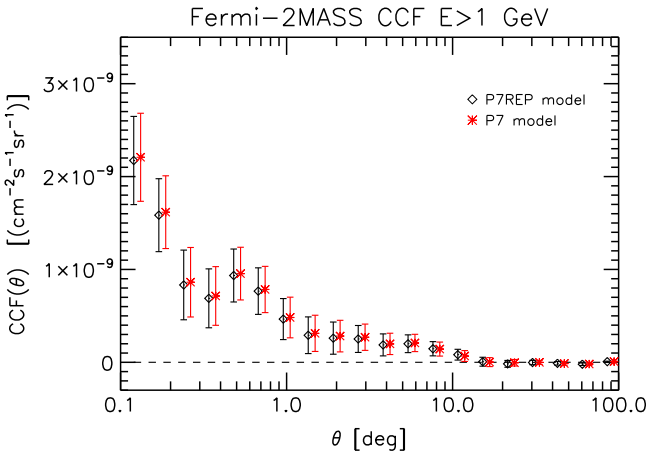

Figure 3. Comparison of *Fermi*-2MASS $E > 1$ GeV CCF for two different Galactic foreground models.

`ring_2year_P76_v0.fits` is tuned to two years of `P7` data and further uses uniform flat patches to model some features of the diffuse sky such as the *Fermi* Bubbles and Loop I. The model `gll_iem_v05_rev1.fit` is based on four years of `P7REP` data and adopts an alternative procedure to account for residual diffuse emission involving templates of residual emission obtained in early stages of model fitting to construct the final model. Because part of the data has been introduced in some form as an a posteriori model component[17] (Ackermann 2014b), the `gll_iem_v05_rev1.fit` model is not recommended for diffuse emission studies. However, because these additional templates only affect regions that are within our masked areas, we can safely also use this model to test the robustness of the results with respect to the modeling of the Galactic emission. Indeed, the comparison between the two models actually shows that they are very similar in our region of interest and give almost identical residuals. This was expected because in our region of interest the diffuse emission is basically accounted for by a single template based on the local H I emission. Not surprisingly, the correlation functions that we obtain when using this model agree at the percent level with the results obtained with the other model, as shown in Figure 3. For definiteness, we set `ring_2year_P76_v0.fits` as our baseline model. Note that, in general, it is not recommended to use the model `ring_2year_P76_v0.fits`, tuned on `P7` data, with `P7REP` data, even though in this particular case, as shown in Figure 3, the differences between the results derived from the two models are small.

Finally, we also subtracted the contributions from solar and lunar emission along the ecliptic. For this purpose we used the appropriate routines of the LAT *Science Tools* and selected options to obtain templates consistent with the data selection and IRF choices described above. The model of the energy and spatial emission from the Sun and Moon have been taken from the related papers (Abdo et al. 2011, 2012), tabulated into the files `solar_profile_v2r0.fits`[18] and `lunar_profile_v2r0.fits`.

The practical procedure we use to obtain the maps of residual photon counts is to use `GaRDiAn` to convolve the Galactic emission model and the Sun and Moon templates with the exposure maps and the PSF, which are then subtracted from the observed counts. Residual flux maps are then obtained by further dividing the residual photon counts by the exposure maps.

Because the Galactic diffuse emission models are not exact, the cleaning is not perfect, and the residual flux maps are still contaminated by spurious signal, especially on large angular scales. The impact on cross-correlation analyses is expected to be small because Galactic foreground emission is not expected to correlate with the extragalactic signal that we want to investigate. Possible counterexamples, like extinction effects, are small and will be discussed in Section 4 in the context of optical extragalactic surveys. Nonetheless, we follow Xia et al. (2011) and apply a cleaning procedure that, using HEALPix tools, removes all contributions from multipoles up to $\ell = 10$, including the monopole and dipole.

The resulting residual photon flux maps, which we dub $\ell 10$ maps, for the three energy ranges considered in this work are shown in the three upper panels of Figure 4. The masked area, also shown in the bottom plot, is represented by the uniform strip across the Galactic plane and further extends around the *Fermi* Bubbles and Loop I. Fluctuations have amplitudes in the range $\pm 1.5 \cdot 10^{-7}$ ph cm^{-1} s^{-1} sr^{-1} for the case $E > 1$ GeV according to the color code shown in the plots. Note that for visualization, but not during the analysis, the maps have been smoothed with a 1° Gaussian filter to remove small-scale Poisson noise. The model seems to slightly over-subtract the γ-ray emission around $(l,b) \sim (175°, -35°)$, corresponding to the gas- and dust-rich (and thus difficult to model) Taurus molecular region. Note, however, that when performing the cross correlation, this region is masked by the further mask specific to the catalog, except in the NVSS case (see below), so no bias in the results is expected from this feature.

4. MAPS OF DISCRETE SOURCES

In this section we describe the different catalogs of extragalactic objects that we cross correlate with the $\ell 10$ maps of the diffuse IGRB obtained after the cleaning procedure described in Section 3.

In this work we have considered five different catalogs: (1) the SDSS DR6 quasar catalog released by Richards et al. (2009) that should trace the FSRQ population, (2) the IR-selected Two Micron All Sky Survey (2MASS) extended source catalog (Jarrett 2000) to trace SFGs, (3) the NRAO VLA Sky Survey (NVSS) catalog of radio galaxies (Condon et al. 1998) that we regard as alternative tracers to the FSRQs, (4) the DR8 SDSS catalog of LRGs (Abdalla et al. 2008), which should trace an intrinsically fainter, more local AGN population like the BL Lacs, and (5) the DR8 SDSS Main Galaxy Sample (Aihara et al. 2011) as a potential additional tracer of SFGs.

The redshift distributions, $dN/d\ln z$, of the various sources are shown in Figure 5 and described in more detail in the next subsections. The various distributions peak at quite different redshifts, with 2MASS representing the most local population and SDSS DR6 QSOs the most distant one. These characteristics in principle enable breaking down the cross-correlation analysis in different redshift ranges, effectively allowing a *tomographic* investigation of the IGRB origin. A detailed description of these catalogs, except the SDSS DR8 Main Galaxy Sample, can be found in Xia et al. (2011). Below we briefly summarize the main features of each sample.

[17] http://fermi.gsfc.nasa.gov/ssc/data/access/lat/Model_details/FSSC_model_diffus_reprocessed_v12.pdf
[18] http://fermi.gsfc.nasa.gov/ssc/data/analysis/scitools/solar_template.html

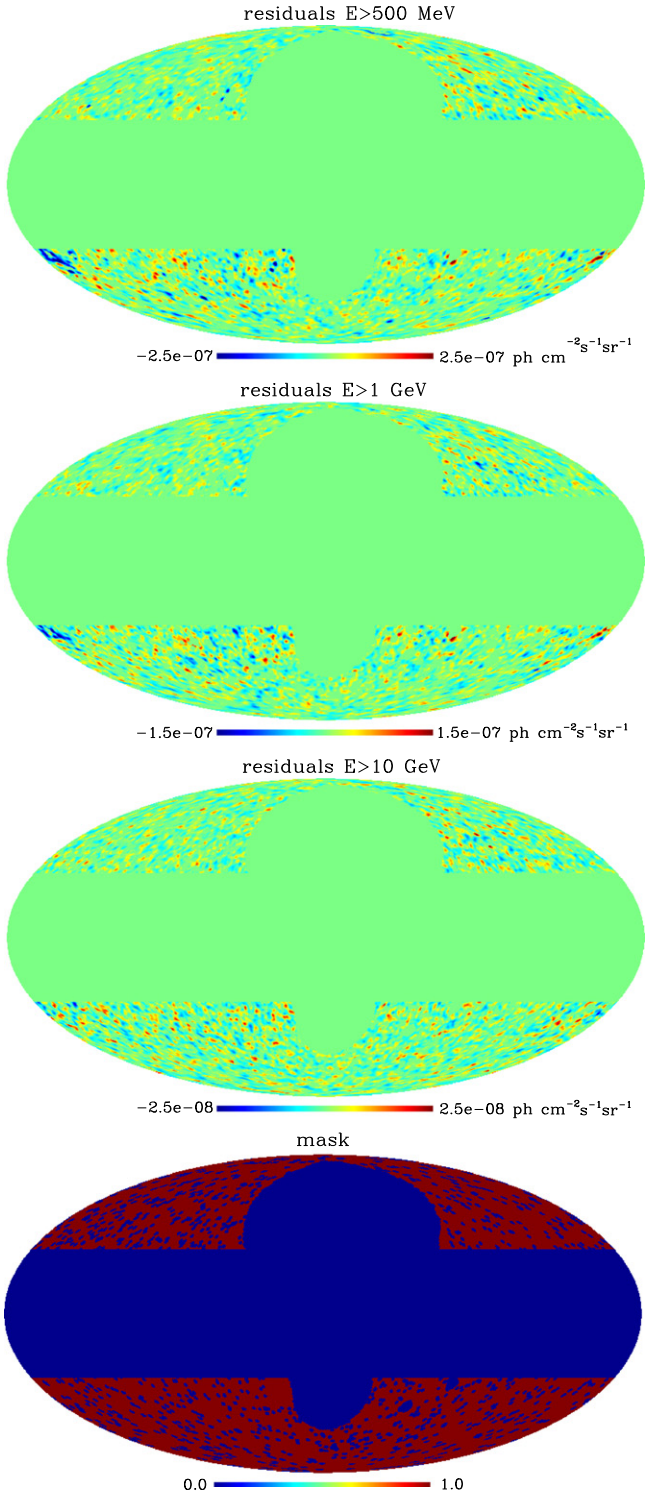

Figure 4. Upper three plots: fluctuations of the residual γ-ray photon flux maps obtained from 60 months of *Fermi*-LAT data for energies $E > 500$ MeV (top), $E > 1$ GeV (second from the top), $E > 10$ GeV (second from the bottom). Foreground emission from Galactic diffuse, Sun, and Moon have been subtracted from the data as well as multipoles as large as $l = 10$. Different colors indicate fluctuations of different amplitude according to the color scheme in the plots. The flat-color areas across the Galactic plane and around the *Fermi* Bubbles and Loop I correspond to the mask and have been ignored in the correlation analysis. The mask, which also accounts for resolved sources, is further shown in the bottom plot. The maps are in Galactic coordinates and have a resolution $N_{\rm side} = 512$. For visualization, but not during the analysis, the maps have been further smoothed with a 1° Gaussian filter to remove small-scale Poisson noise.

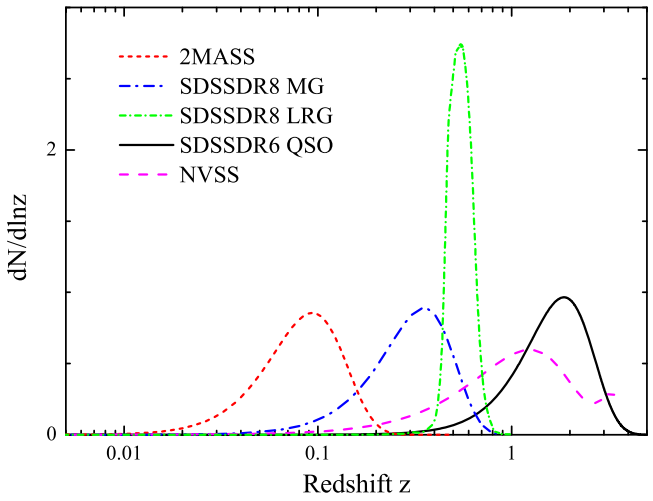

Figure 5. Redshift distributions, $dN/d\ln z$, of the different types of objects considered for our cross-correlation analysis: SDSS DR6 QSOs (black, continuous line), 2MASS galaxies (red, short-dashed), NVSS galaxies (magenta, long-dashed), SDSS DR8 LRGs (green, short, dot-dashed), and SDSS DR8 Main Galaxy Sample (blue, long, dot-dashed)

4.1. SDSS DR6 QSO

The SDSS DR6 quasar catalog (Richards et al. 2009; hereafter DR6 QSO) contains about $N_{\rm q} \approx 10^6$ quasars with photometric redshifts between 0.065 and 6.075, covering almost all of the north Galactic hemisphere plus three narrow stripes in the south, for a total area of 8,417 deg^2 (corresponding to ~20% of the whole sky). The DR6 QSO data set extends previous similar SDSS data sets (Richards et al. 2004; Myers et al. 2006). The main improvements are due to the fact that this catalog contains QSOs at higher redshift and also contains putative QSOs flagged as objects with ultraviolet excess (UVX objects). We refer the reader to Richards et al. (2009) for a detailed description of the object selection performed with the nonparametric Bayesian classification kernel density estimator (NBC-KDE) algorithm.

In this work we used objects listed in the electronically published table with a "good object" flag in the range [0,6]. The higher the value, the more probable the object is a real QSO (Richards et al. 2009). We only consider the quasar candidates selected via the UV-excess-only criteria "uvxts = 1," i.e., objects clearly showing a UV excess, which represents a characteristic QSO spectral signature. After this selection we are left with $N_{\rm q} \approx 6 \times 10^5$ quasar candidates.

In order to determine the actual sky coverage of the DR6 survey and generate the corresponding geometry mask, we Monte Carlo sample the observed areas with a sufficiently large number of objects using the DR6 database to ensure roughly uniform sampling on the SDSS CasJobs[19] website. Following Xia et al. (2009), we combine the pixelized mask geometry with a foreground mask obtained by removing all pixels with the g-band Galactic extinction $A_{\rm g} \equiv 3.793 \times E(B-V) > 0.18$ to minimize the impact of Galactic reddening.

The redshift distribution function dN/dz of the DR6 QSO sample in Figure 5 is well approximated by the analytic

[19] http://skyserver.sdss3.org/CasJobs/

function

$$\frac{dN}{dz}(z) = \frac{\beta}{\Gamma\left(\frac{m+1}{\beta}\right)} \frac{z^m}{z_0^{m+1}} \exp\left[-\left(\frac{z}{z_0}\right)^\beta\right], \quad (19)$$

where three free parameter values are $m = 2.00$, $\beta = 2.20$, and $z_0 = 1.62$ (Xia et al. 2009). In addition, to calculate theoretical predictions (Equation (12)) we follow Giannantonio et al. (2008) and Xia et al. (2009) and assume a constant, linear bias model $b_S = 2.3$.

4.2. 2MASS

The 2MASS extended source catalog is an almost-all-sky survey that contains ~770,000 galaxies with mean redshift $\langle z \rangle \approx 0.072$. In this work we have selected objects with apparent isophotal magnitude $12.0 < K'_{20} < 14.0$, where the prime symbol indicates that magnitudes are corrected for Galactic extinction using $K'_{20} = K_{20} - A_k$, with $A_k = 0.367 \times E(B - V)$. We select objects with a uniform detection threshold (use_src = 1), remove known artifacts (cc_flag $\neq a$ and cc_flag $\neq z$), and exclude regions with severe reddening, $A_k > 0.05$ (Schlegel et al. 1998). This procedure leaves approximately 67% of the sky unmasked. The redshift distribution of the selected objects can be approximated with the same functional form used for DR6 QSOs with parameters $m = 1.90$, $\beta = 1.75$, and $z_0 = 0.07$ (Giannantonio et al. 2008). The value of the linear bias of 2MASS galaxies has been set equal to $b_S = 1.4$ (Rassat et al. 2007).

The possible incompleteness of the 2MASS catalog at faint magnitudes might affect our cross-correlation analysis. For this reason we have repeated the analysis using smaller 2MASS samples with more conservative magnitude cuts: $K'_{20} < 13.9$, $K'_{20} < 13.7$, and $K'_{20} < 13.5$. More specifically, we computed the two-point CCF between these 2MASS maps and the *Fermi* $E > 1$ GeV residual map and find that the CCF results do not change significantly: the possible incompleteness of the larger catalog does not induce any spurious correlation signal. Therefore, in our analysis we use the larger 2MASS sample cut at $K'_{20} = 14$.

4.3. NVSS

The NVSS (Condon et al. 1998) offers the most extensive sky coverage among the catalogs considered here (82% of the sky to a completeness limit of about 3 mJy at 1.4 GHz) and contains 1.8×10^6 sources. We include in our analysis only NVSS sources brighter than 10 mJy because the surface density distribution of fainter sources suffers from declination-dependent fluctuations (Blake & Wall 2002). We also exclude the Galactic plane strip at $|b| < 5°$ where the catalog may be substantially affected by Galactic emissions. This additional cut is redundant with the one applied to the LAT maps. It is applied to compute the NVSS source surface density at this flux threshold, which turns out to be 16.9 deg^{-2}.

The redshift distribution at this flux limit has been determined by Brookes et al. (2008). Their sample, complete to a flux density of 7.2 mJy, contains 110 sources with $S \geqslant 10$ mJy, of which 78 (71%) have spectroscopic redshifts, 23 have redshift estimates from the $K - z$ relation for radio sources, and nine were not detected in the K band and therefore have a lower limit to z. We adopt the smooth parameterization of this redshift distribution given by de Zotti et al. (2010):

$$\frac{dN}{dz}(z) = 1.29 + 32.37z - 32.89z^2 + 11.13z^3 - 1.25z^4. \quad (20)$$

For the bias of the NVSS sources we adopt a linear model $b_S = 1.8$ (Giannantonio et al. 2012). Note that a comprehensive analysis of the NVSS autocorrelation function is provided by Xia et al. (2010).

4.4. SDSS DR8 LRG

To sample the spatial distribution of the LRGs, we use the photometric LRG catalog from the final imaging of SDSS DR8 instead of the MegaZ LRG sample because the latter has an excess of power on large scales with respect to the ΛCDM model (Thomas et al. 2011). The sample used here was selected using the same criteria as the SDSS-III BOSS "CMASS" sample defined in Ross et al. (2011). They applied color cuts to account for seeing effects, dust extinction, sky brightness, air mass, and possible stellar contamination.

Ho et al. (2012) further excluded regions where $E(B - V) > 0.08$ for the dust extinction, when the seeing in the i band $> 2''.0$ in FWHM, and additionally masked regions are affected by bright stars. This selection yields a sample with $\sim 8 \times 10^5$ LRGs and leaves approximately 22% of the sky unmasked.

Photometric redshifts of this sample are calibrated using about 100,000 BOSS spectra as a training sample for the photometric catalog. The resulting redshift range is $0.45 < z < 0.65$ with a mean redshift of $\bar{z} \sim 0.5$, as shown in Figure 5. Also in this case, and following Ross et al. (2011) and Hernández-Monteagudo et al. (2014), we assume a linear bias parameter of $b_S = 2.1$.

4.5. SDSS DR8 Main Galaxy Sample

We consider the sample of photometrically selected "main" galaxies extracted from the SDSS DR8 catalog. The selection is performed according to Giannantonio et al. (2008): we consider objects with extinction-corrected r-band magnitude in the range $18 < r < 21$ and with redshifts in the range $0.1 < z < 0.9$. Further, we only include objects with redshift errors smaller than $\sigma_z = 0.5z$, which leaves us with about 4.2×10^7 sources with redshifts distributed around a median value of $\bar{z} \sim 0.35$. In addition, we adopt a foreground mask to minimize the effect of Galactic extinction by excluding all galaxies within pixels in which the r-band Galactic extinction $A_r > 0.18$. Finally, we have about 35 million sources for the analyses.

The redshift distribution dN/dz of the SDSS galaxies can be approximated with the same functional form used for DR6 QSOs and 2MASS galaxies with parameters $m = 1.5$, $\beta = 2.3$, and $z_0 = 0.34$. Following Giannantonio et al. (2012) we use a constant bias parameter of $b_S = 1.2$.

5. CROSS-CORRELATION ANALYSIS

In this section we describe the cross correlation between the residual IGRB flux maps and the angular distribution of extragalactic sources in the catalogs described in Section 4. All of the maps we use are in HEALPix format with a resolution of $N_{\rm side} = 512$.

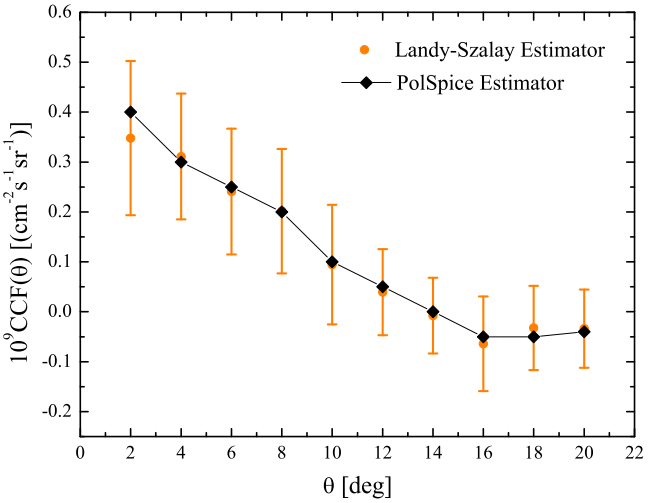

Figure 6. CCFs between *Fermi* maps $E > 1$ GeV and 2MASS galaxies computed using PolSpice (black diamonds) and LS (orange dots) estimators. Error bars are computed by using the Jackknife resampling method.

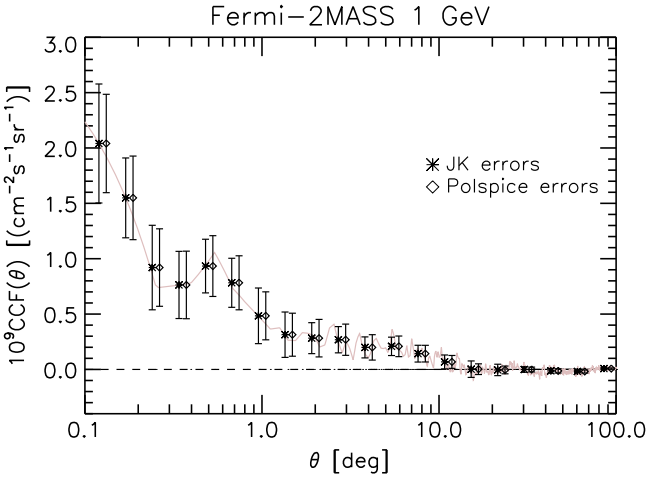

Figure 7. Comparison of the error bars of the CCF between *Fermi* maps $E > 1$ GeV and 2MASS galaxies computed using the PolSpice covariance matrix and the Jackknife resampling method. CCFs for the Jackknife subsamples are calculated with the PolSpice estimator. The thin line shows the unbinned CCF.

Our analysis relies on the latest version v02-09-00 of PolSpice[20], a publicly available statistical tool to estimate both the angular two-point CCF $\hat{C}^{\rm fg}(\theta)$ and the cross-angular power spectrum $\hat{C}^{\rm fg}(l)$ of any two diffuse data sets, f and g, pixelized on a sphere. The code is based on the fast spherical harmonic transforms allowed by isolatitude pixelizations and automatically corrects for the effects of the masks. Data sets and masks in the form of HEALPix sky maps are input to the code. The output consists of the angular two-point correlation function, the angular power spectrum, and its covariance matrix, which account for the effect of incomplete sky coverage and from the nominal beam window function and average pixel function. In our calculations, we perform the correlation analyses in the multipole and angular ranges $\ell \in [10, 1000]$ and $\theta \in [0.^\circ1, 100^\circ]$ for CAPS and CCF, respectively.

The PolSpice estimator has been described in detail and thoroughly tested as a tool to measure both the spectrum and the covariance matrix of a sky map (Szapudi et al. 2001; Chon et al. 2004; Efstathiou 2004; Challinor & Chon 2005). Because in our previous work (Xia et al. 2011) we based our analysis on the Landy–Szalay (LS) estimator (Landy & Szalay 1993) and computed errors using a Jackknife (JK) resampling technique (see below), we have checked the consistency of the two approaches and compared the outputs from the different estimators.

In Figure 6 we compare the CCF between 2MASS and *Fermi* data above 1 GeV estimated using PolSpice with the same CCF estimated using LS. The agreement between the two methods is at about 10% in the first angular bin and a few percent in the other bins, well within the amplitude of the 1σ random errors, and demonstrates that our results are robust to the choice of the estimator for two-point statistics. Note that, only in this particular case, the angular binning is linear, as dictated by the LS estimation method, which, being particularly computationally expensive, is applied using maps with a coarse $N_{\rm side} = 64$ pixelization.

Analogously, in Xia et al. (2011), in order to estimate the covariance matrix we used the JK resampling method (Scranton & Johnston 2002), which divides the data into M patches and estimates the covariance matrix as

$$C^{\rm JK}_{\theta\theta'} = \frac{M-1}{M}\sum_{k=1}^{M}\left[\xi_k^{\rm obs}(\theta) - \xi^{\rm mean}(\theta)\right] \times \left[\xi_k^{\rm obs}(\theta') - \xi^{\rm mean}(\theta')\right], \quad (21)$$

where $\xi_k^{\rm obs}(\theta)$ is the correlation function estimated in the kth subsample and $\xi^{\rm mean}(\theta)$ is the mean correlation function over the M subsamples. PolSpice provides an estimate for the covariance matrix of the CAPS, $\bar{M}_{\ell_1\ell_2}$ (Efstathiou 2004). From this, and using the procedure described in the Planck collaboration et al. (2013b), we obtain the covariance matrix for the CCF:

$$C^{\rm PS}_{\theta\theta'} = \sum_{\ell}\sum_{\ell'}\frac{2\ell+1}{4\pi}\frac{2\ell'+1}{4\pi}P_\ell(\cos(\theta))P_{\ell'}(\cos(\theta'))\bar{M}_{\ell_1\ell_2}, \quad (22)$$

which is then averaged over the angular separations θ and θ' within each bin to obtain a binned covariance matrix. In Figure 7 we show the same CCF plotted in Figure 6 with two sets of error bars corresponding to the (square root of the) diagonal elements of the Polspice and JK covariance matrices. The agreement between the two sets of error bars is excellent, as is the agreement between the off-diagonal elements (not shown), for which the largest difference does not exceed 10%.

6. VALIDATION AND CHECKS

In this section we assess the validity of the different steps of our analysis and assess the robustness of our results. For brevity we only present a subset of cross-correlation analyses involving the *Fermi*-LAT and 2MASS maps. However, we have performed the very same robustness tests for all cross-correlation analyses described in this work.

6.1. Test with Different Galactic Diffuse Models

The cleaning procedure described in Section 3 is potentially prone to systematic errors that may affect the correlation

[20] See http://www2.iap.fr/users/hivon/software/PolSpice/

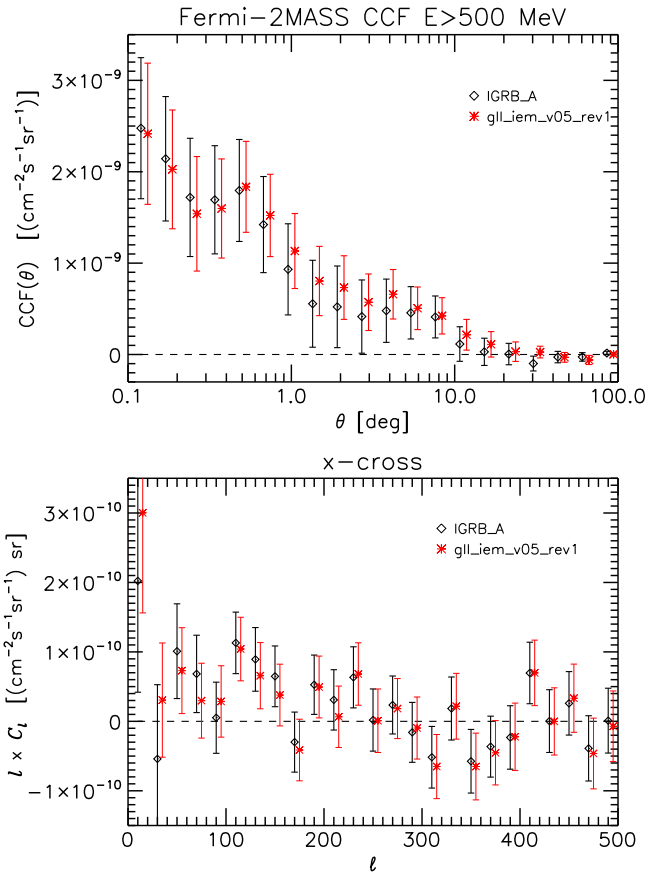

Figure 8. Comparison of *Fermi*-2MASS E > 500 MeV CCF (lower panel) and CAPS (upper panel) for two different Galactic foreground models.

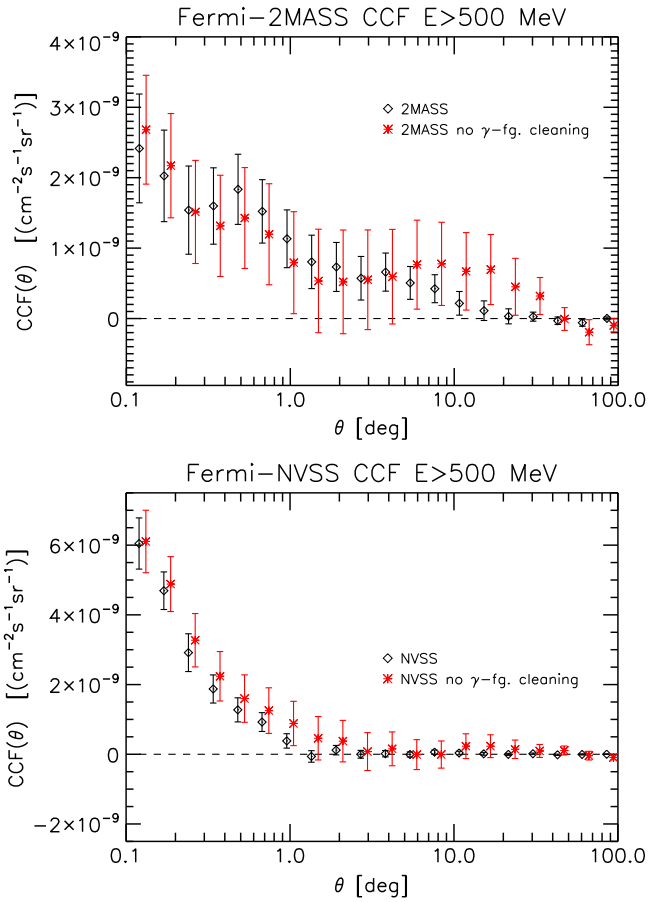

Figure 9. Comparison between CCFs with and without Galactic foreground cleaning for the $E > 500$ MeV *Fermi*-2MASS case (upper panel) and *Fermi*-NVSS case (lower panel).

analysis. We searched for these systematic effects by using two different emission models, also described in Section 3, to correct for Galactic emission. The results show that the correlation signal does not change appreciably when using either model.

Given the importance of this issue, we performed a third test in which we adopted an alternative Galactic emission model fully based on GALPROP. In this test, we used the GALPROP "model A" described in the *Fermi*-LAT collaboration paper (Ackermann 2014a), which is one of the models used to assess the systematic uncertainties in the derivation of the IGRB energy spectrum due to the Galactic diffuse emission modeling. The model consists of two components: inverse Compton emission and gas emission (pion decay plus bremsstrahlung). Together with an isotropic template, we normalize this three-component model by fitting the high Galactic latitude γ-ray sky (more precisely using the mask of Figure 4), leaving the normalization of all of the three components free to vary in the fit. The tuned model is adopted as in Section 3 to clean the Galactic diffuse emission. The usual ℓ10 cleaning procedure is then used to derive the final residual map from which we calculate the CCFs and CAPS. In Figure 8 we compare the CCFs and CAPS between γ-rays and 2MASS for the `gll_iem_v05_rev1.fit` model already used in Section 3 to the alternative model results. From the plots it can be seen that some difference exists at low multipoles (below ∼40). However, the difference is within the 1σ error bars and decreases at small scales (high multipoles), where the signal is higher. This shows that the results of our cross-correlation analysis are robust with respect to the modeling of the Galactic diffuse emission.

Finally, for completeness, we show in Figure 9 the CCF between the $E > 500$ γ-ray map *without any foreground cleaning* and 2MASS and NVSS. The plot shows that removing the Galactic emission is important to reduce the size of the error bars. On the other hand, even without any removal, the correlation is not biased, as expected given that no correlation between the Galactic emission and LSS is in principle present. This in turn also implies that an imperfect Galactic emission removal would similarly not introduce any bias, although the error bars could be nonoptimal.

6.2. Use of Different Galactic and Point-source Masks

Incorrect masking is another potential source of systematic errors. To tests the robustness of our results against the choice of the mask and to check for the possible presence of Galactic foreground contamination, we have varied the Galactic latitude cut from $b = 20°$ to $b = 60°$ in steps of $\Delta b = 10°$, as in Xia et al. (2011). In addition, we performed the cross-correlation analysis using only the northern or the southern hemispheres of the maps. In all of the cases we explored, the results turned out to be consistent within the errors, which clearly increase with the size of the masked region.

Inefficient excision of discrete sources is yet another potential concern. We estimate its impact on our analysis by using different masks corresponding to excluding sources from

two different catalogs: 2FGL and a preliminary version of the 3FGL. Moreover, to excise sources we used two criteria: (1) we masked out circles of 1° radius centered on all sources, and (2) we masked out circles of 2° radius for the 500 brightest sources and circles of 1° radius for the others. The results of the correlation analyses turned out to be insensitive to the choice of the source mask. Clearly, increasing the size of the masked areas decreases the risk of contamination but also decreases the significance of the correlation signal. Therefore, in an attempt to compromise between maximizing the statistical significance and minimizing contamination in the different cross-correlation analyses, we proceed as follows: (1) for the cross correlation with the NVSS and 2MASS catalogs and for $E > 500$ MeV, which represents the case of a large surveyed area and large contamination due to the broadening of the *Fermi*-LAT PSF below 1 GeV, we adopt the most conservative source mask based on the 3FGL catalog and with larger (2° radius) circles, (2) for NVSS and 2MASS and $E > 1$ GeV, with a lower contamination, we use 3FGL and 1°, and (3) for all SDSS-based catalogs, which have the smallest sky coverage, we have considered a less aggressive 2° 2FGL mask for $E > 500$ MeV and (4) a 1° 2FGL mask for higher energy cuts.

While the results are robust against the choice of the source mask, their significance can change appreciably. For the NVSS and 2MASS catalogs, using different source masks varies the size of the error bars by 20–30%, so the choice of the mask is not critical in these cases. For the various SDSS-based catalogs, instead, using 3FGL rather than 2FGL significantly reduces the significance of the results, and, for this reason, we opt for the least conservative mask.

6.3. Robustness to γ-Ray Event Conversion

In our analysis, to maximize statistics, we consider both front- and back-converting γ-ray events. However, the two types of events have different characteristics; most notably, back-converting events have a larger PSF. To check whether the nature of the conversion affects our results, we divided the γ-ray data sets into two subsamples, each one containing only front-converting or back-converting events. The resulting maps were cleaned using the same procedure, i.e., convolving the various model templates with the appropriate IRFs.

As a result of halving the number of events, the significance of the correlation is somewhat reduced for each subsample, in particular for the SDSS catalogs. Within the increased error bars, however, we do not observe any bias among the three data sets (front only, back only, and front plus back). We conclude that possible systematic differences between the front and back data sets are below the present statistical uncertainties, and we thus decided to perform the analysis using both types of events jointly.

6.4. Sensitivity to the PSF of the Detector

As we shall see, a significant fraction of the cross-correlation signal observed in our analysis originates from small angular scales comparable to the angular extent of the LAT PSF. As a consequence, we need to estimate the effect of the PSF and include it explicitly in our analysis.

The PSF smears out the signal from small to large angular scales, hence reducing the amplitude of both the CCF and CAPS at small angular separations and large multipoles, respectively. However, this effect can be modeled if the PSF of the telescope, or the instrumental beam, is measured accurately. In the case of the LAT, the beam depends on the energy, and the PSF can be determined either from observations by stacking the images of bright point sources (Ackermann et al. 2013) or from a Monte Carlo simulation of the detector performance (Ackermann et al. 2012b). The characterization of the PSF has improved with the `P7` and `P7REP` data release, and a discrepancy at high energies (greater than a few gigaelectronvolts) between the Monte Carlo PSF and the in-flight PSF present for the `P6` data is now significantly reduced (Ackermann et al. 2012b). The beam shape is part of the IRFs and can be estimated using the LAT Science Tools. In particular, we used the tool `gtpsf` to obtain the PSF as a function of energy and angular separation of the photon from its true arrival direction. Because the latter is a function of one angle only, we are neglecting the ellipticity of the beam, which, in any case, turns out to be negligible. It is more convenient to consider the effect of the beam in harmonic space, where it can be expressed as a multiplication, rather than in configuration space, where it would be a convolution. Indeed, if $C_l(E)$ represents the true CAPS at a given energy, then the measured one is $\tilde{C}_l(E) = W_l(E) C_l(E)$, where $W_l(E)$ is the beam window function. The latter can be expressed as a Legendre transform:

$$W_l(E) = 2\pi \int_{-1}^{1} d\cos(\theta)\, P_l(\cos\theta) \mathrm{PSF}(\theta, E), \qquad (23)$$

where $P_l(x)$ is the Legendre polynomial of order l and $\mathrm{PSF}(\theta, E)$ is the shape of the beam. Because we are analyzing data integrated over a fairly large energy bin within which the PSF can vary significantly, the effective window function for the bin will be a weighted average over the energy range

$$W_l(E_1 < E < E_2) = \frac{1}{N} \int_{E_1}^{E_2} dE\; W_l(E) \frac{dN}{dE}(E), \qquad (24)$$

where dN/dE represents the differential number of photon counts in the region of the sky we want to analyze, $N = \int_{E_1}^{E_2} dE\, (dN/dE)(E)$, and $[E_1, E_2]$ is the energy bin considered. Finally, there is a further window function to take into account because we use a pixelized map, which is the pixel window function itself, $W_{\mathrm{pix},l}$. The pixel window function depends on the size of the pixel (and on the shape of the pixel itself). It can be easily extracted using the appropriate HEALPix tools. The final window function is then given by $W_l(E_1 < E < E_2) \cdot W_{\mathrm{pix},l}$. The effective window functions for the three energy ranges considered in this work are shown in Figure 10.

Once determined, the effective window function can be fed into PolSpice to recover the true CAPS and the CCF from the measured ones. However, we find that the algorithm used to perform the deconvolution is quite unstable, especially in the CCF reconstruction. For this reason we take the opposite approach, and instead of deconvolving the signal, we convolve the model predictions and compare them to the measurement. More explicitly, if C_l is the model CAPS and $W_l^{\Delta E}$ is the estimated effective window function in the bin ΔE, then the convolved CAPS is

$$C_l^W = C_l\, W_l^{\Delta E}, \qquad (25)$$

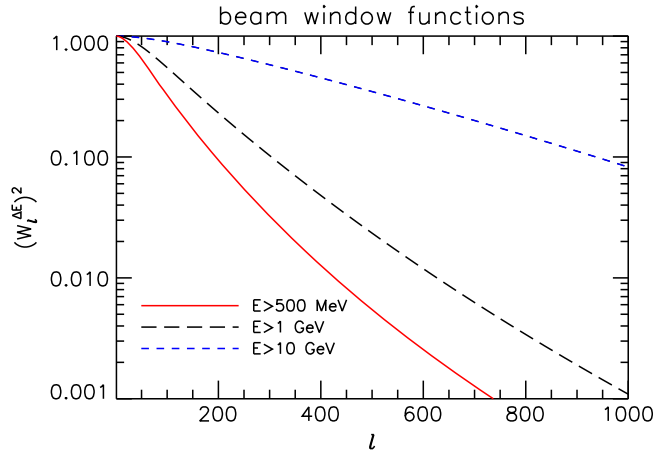

Figure 10. Effective squared window functions of the beam, $(W_l^{\Delta E})^2$, in the three energy ranges $E > 500$ MeV (red, solid), $E > 1$ GeV (black, long-dashed), and $E > 10$ GeV (blue, short-dashed).

and, analogously, the convolved CCF is

$$\mathrm{CCF}^W(\theta) = \sum_l \frac{(2\,l+1)}{4\pi} C_l^W P_l(\cos\theta). \quad (26)$$

To test the validity of our PSF correction procedure, we proceed as follows: (1) we consider the high Galactic latitudes $|b| > 30°$ region of the sky (to reduce the impact of the Galactic contamination) but without masking the locations of known point sources, (2) we calculate the auto power spectrum for this region (APS, not the CAPS), and (3) we then apply the pipeline described in the above paragraphs to obtain an empirical estimate of the window function in each of the three energy bands considered. The resulting APS in this case will be dominated by the bright point sources and is expected to match the Legendre transform of the window function (squared): $(W_l^{\Delta E})^2$. The results are shown in the three panels of Figure 11. Because the APS of the map, represented by black asterisks, is expected to match the window function, then the flatness of the ratio between the APS and $(W_l^{\Delta E})^2$ indicates that our hypothesis is correct and that our estimated window function is robust in all three energy ranges and at all multipoles, apart from a small overestimation at very high l. Note that, in contrast to Ackermann (2012a) where the γ-ray APS is also considered, we neglect here the effect of Poisson shot noise, which is subdominant at all multipoles, given the very strong APS signal from bright point sources. Instead, no shot noise term needs to be considered for CAPS because the uncorrelated noises from the two maps being cross correlated do not produce a net nonnull noise CAPS, contrary to the APS case. The slight overestimate of the APS PSF correction in the 700–1000 l range at the level of 20–30% turns into a 10–15% systematic effect for the CAPS, where the PSF correction is given by $W_l^{\Delta E}$ rather than $(W_l^{\Delta E})^2$. On the other hand, as we will see in Section 7, all CAPS are compatible with zero in this multipole range, except for a weak signal for NVSS, so the error is dominated by statistical random errors. We will thus neglect the above systematic effect.

6.5. CR Contamination

The IGRB maps we obtained in Section 3 contain, in addition to true γ-ray events, some contamination from cosmic rays that have been misclassified as γ-rays. With the `P7REP_CLEAN` event selection that we used, the CR contamination is at the level of 15–20% of the IGRB flux above 1 GeV, rising to 40–50% at 500 MeV (see Figure 28 in Ackermann et al. 2012b). Because the contaminant cosmic rays are not expected to correlate with cosmological structures, they do not induce systematic errors in our analysis. Instead, they will only increase random error because the signal-to-noise ratio of the γ-ray signal will be reduced. Nonetheless, to verify this hypothesis, we used the IGRB maps produced with the `P7REP_ULTRACLEAN` selection, which has a slightly reduced CR contamination with respect to `P7REP_CLEAN`, at the level of 10–15% of the IGRB flux above 1 GeV and 30–40% at 500 MeV (Ackermann et al. 2012b). We computed CAPS and CCFs for this case and found that the results are indistinguishable from those obtained with the `P7REP_CLEAN` selection. A more stringent test could be performed using special event-selection criteria designed to further reduce the CR contamination for specific studies of the IGRB spectrum, as in Abdo et al. (2010a) and Ackermann (2014a). These selections should in principle allow us to reduce the error bars. However, these selection criteria introduce more conservative cuts to reduce the background. Consequently, the benefit of the better cleaning is counteracted by the effective area reduction, resulting typically in no effective reduction of the error bars. Indeed, the optimal selection should balance purity and photon statistics. However, the search for such a compromise is beyond the scope of our analysis.

6.6. No-signal Tests

To check the robustness of the results, we performed further tests using mock catalogs with no cross correlation with LSS, verifying that the computed CCFs are compatible with a null signal.

In Figure 12 we show the cross correlation between the *Fermi* $E > 500$ MeV map and three mock realizations of each of the three catalogs 2MASS, SDSS Main Galaxy Sample, and NVSS. The correlations are compared with the ones with the true catalogs. For each catalog, two mock realizations were built, scrambling the Galactic coordinates of each galaxy of the sample, changing $b \rightarrow -b$ in one case and $l \rightarrow -l$ in the other. These two realizations preserve the intrinsic clustering of the catalog but remove the cross correlation with LSS. To compute the CCF we use the corresponding scrambled coordinate mask of the given catalog. A third realization was performed, creating a Monte Carlo catalog that redistributed the galaxies of the catalog randomly over the sky area covered by the catalog. In this case the new catalog contains no intrinsic clustering. To compute the CCF, we use in this case the original catalog mask.

The plots in Figure 12 show that the correlation present for the true catalog disappears when the mock catalogs are used, as expected. We note that the size of the error bars are typically smaller than the true catalog CCF error bars when the Monte Carlo catalog is used, but not in the case of the scrambled-coordinates catalogs. This is likely because the Monte Carlo catalogs do not contain intrinsic clustering, as opposed to the true and scrambled-coordinates catalogs, and this emphasizes the importance of the error cross checks we performed in Section 5.

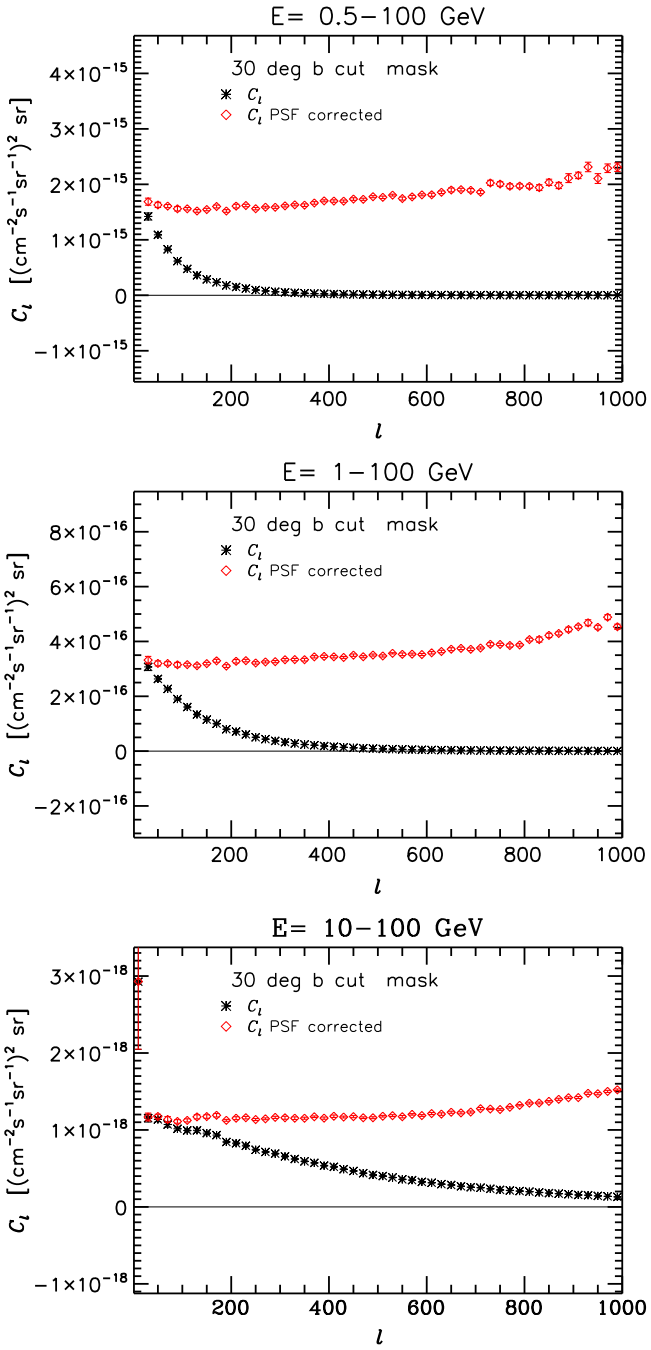

Figure 11. Measured auto power spectrum of the LAT maps at $|b| > 30°$ (black asterisks) and ratio between the APS and the average beam window squared $(W_l^{\Delta E})^2$ (red open dots) for three energy bands.

7. RESULTS

In this section we show the results of our cross-correlation analysis both in configuration space (i.e., the angular CCF) and in harmonic space (i.e., the CAPS) obtained by combining the cleaned *Fermi*-LAT IGRB maps with the angular distributions of objects in the various catalogs presented in Section 4. The analysis is carried out in three different energy bands, and the results are compared with theoretical predictions obtained under the assumption that the extragalactic, diffuse IGRB signal is generated by a combination of three different types of unresolved sources, BL Lacs, FSRQs, and SFGs, as described in Section 2.1. As explained in Section 6.4, we do not attempt to deconvolve the measured correlation function from the instrument PSF. The predicted correlations are, instead, convolved with the PSF itself and then compared with the measurements. As we anticipated in previous sections, we take the relative contributions of the different types of sources to the IGRB as a free parameter of the model. In the next section we will perform a quantitative analysis to constrain these parameters. In this section and in the following plots, we use a priori models assuming that each source class contributes 100% of the observed IGRB spectrum, with the purpose of an equal-footing and quick comparison between the data and the different models. In fact, we assume a reference IGRB to normalize the model predictions because, as already discussed in the previous sections, the results of our correlation analysis do not depend on the measured IGRB and its uncertainties. More precisely, our reference IGRB is $I(E) = I_0(E/E_0)^{-2.4}$ with $E_0 = 100$ MeV and $I_0 = 1.44 \times 10^{-7}$ MeV cm^{-2}s^{-1}sr^{-1}, which is consistent with the measured one (Abdo et al. 2010a). As a result, the integrated intensities of the IGRB in the three energy ranges that we consider here are 1.0×10^{-6}, 4.0×10^{-7}, and 1.5×10^{-8} cm^{-2}s^{-1} sr^{-1} for $E > 500$ MeV, $E > 1$ GeV, and $E > 10$ GeV, respectively.

In the following section we illustrate the results of cross correlating the individual catalogs. Unlike in the analysis presented by Xia et al. (2011), we now observe a significant cross-correlation signal that, in Section 8, we compare with model predictions to infer the nature of the sources that contribute to the IGRB.

To assess the significance of the signals, we use the usual likelihood ratio test, assuming a Gaussian likelihood $L \propto \exp(-\chi^2/2)$ with

$$\chi^2 = \sum_{ij} \Big(d_i - m_i\Big(f_{\rm sfg}\Big)\Big) C_{ij}^{-1} \Big(d_j - m_j\Big(f_{\rm sfg}\Big)\Big), \qquad (27)$$

where C_{ij} is the covariance matrix among the different angular or multipole bins i computed using PolSpice, d_i represents the data, i.e., the CCF or CAPS measured at the bin i, and $m_i(f_{\rm sfg})$ is the model prediction, which depends on the parameter $f_{\rm sfg}$, i.e., the normalization of the model CCF or CAPS (see also Section 8). We use as a model the SFGs1 model with free normalization, although we note that the $\chi^2_{\rm bf}$ and the significances calculated using the other models are very similar. In Equation (27) the sum extends over 10 angular bins logarithmically spaced between $\theta = 0.^\circ1$ and $100°$ for the CCF and over 10 multipole bins logarithmically spaced between $\ell = 10$ and $\ell = 1000$ for the CAPS. The resulting test statistics (TS) in this case simplifies as $\mathrm{TS} = \chi_0^2 - \chi^2_{\rm bf}$, where χ_0^2 is the χ^2 of the data with respect to the null hypothesis (CCF$(\theta) = 0$ or CAPS$(\ell) = 0$) and $\chi^2_{\rm bf}$ is the best-fit χ^2 of the data with respect to the model. The derived TS significances are shown in Table 2 for the CCFs and Table 3 for the CAPS and are commented upon in the subsections below for each catalog. The tables also report $\chi^2_{\rm bf}$ and the significances in sigmas assuming $\sigma = \sqrt{\mathrm{TS}}$.

7.1. One-halo-like Term

As discussed in Section 2.3, a further contribution to the cross correlation can arise from a *one-halo* term or if part of the

sources of a given catalog are also themselves γ-ray emitters. We denoted these terms collectively as *one-halo*-like. To test empirically the possibility of the presence of a *one-halo*-like term, we adopt the following procedure. For each catalog and for each energy band, we perform a two-parameter fit using a similar χ^2 as in Equation (27), but modeling m_i as the sum of the SFGs1 model with free normalization plus a further term proportional to the PSF profile, i.e., $\propto W_\ell^{\Delta E}$ for the CAPS, and to the related harmonic transform for the CCF. The latter is representative of a correlation at zero angular separation, which is spread at larger angular scales by the effect of the PSF, as expected for a *one-halo*-like term. Again, the results change only marginally if a model different from the SFGs1 model is used.

In Figure 13 we show the one-dimensional χ^2 of the normalization of the *one-halo*-like term profiled over the remaining parameter, i.e., the function obtained from $\chi^2(f_{\rm sfg}, f_{1\,\rm h})$ after minimizing over $f_{\rm sfg}$. The plots refer to the fit to the CCFs. A fit to the CAPS gives similar results. It can be seen that, for all of the energy bands and the four catalogs SDSS DR6 QSO, 2MASS, SDSS LRGs, and SDSS MG, the significance of this extra term is typically below 1σ, reaching the largest significance of little more than 1σ only in the case of the correlation of 2MASS with γ-rays above 1 GeV. The only exception is the NVSS case, where, clearly, a strong preference for a *one-halo*-like term is present. We will discuss further the NVSS case in the dedicated section below, whereas, given the lack of significant indications of the presence of *one-halo*-like contributions, we will not consider the other catalogs further in the following and in the global fitting described in Section 8.

7.2. Cross Correlation with SDSS DR6 QSOs

The DR6 QSO catalog contains AGNs at high redshifts that should preferentially trace bright FSRQs, whose redshift distribution also extends to high redshifts. The results of the cross-correlation analysis are shown in Figure 14. For readability, in all of the plots in this and the following sections, we only show the predictions for the BLLacs1 model because the predictions for the BLLacs2 model are rather similar. The upper panels show the CAPS in three energy bands (increasing from left to right). We plot the corresponding CCFs in the lower panels. At small angular scales, $\theta < 1^\circ$, we observe a cross-correlation signal that is more significant in the low-energy band ($\sim 4.5\sigma$ for the CCF and $\sim 5\sigma$ for the CAPS), where photon statistics are higher. The fact that a weaker signal (2–3σ) is also present for $E > 1$ GeV suggests that the cross-correlation is genuine and not an artifact of systematic errors in the cleaning procedure.

The observed CCF is perfectly consistent with the theoretical predictions of all of the a priori models considered: BL Lacs, FSRQs, and SFGs for all three energy ranges. This is not entirely surprising because the $dI(>\mathrm{E})/dz$ of all of these models

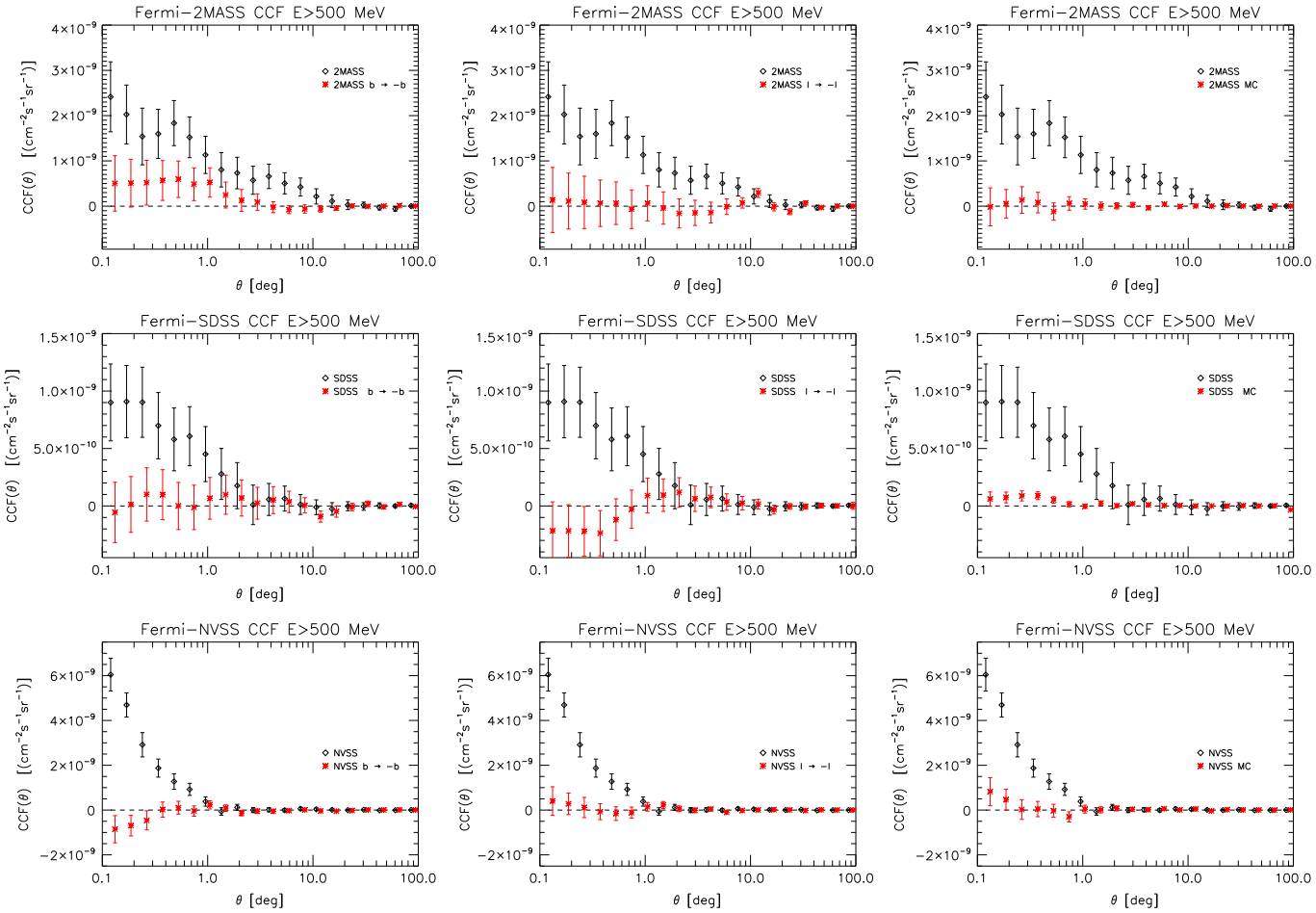

Figure 12. Cross correlations between the *Fermi* $E > 500$ MeV map and three mock realizations of each of the three catalogs 2MASS, SDSS Main Galaxy Sample, and NVSS, compared with the correlations with the true catalogs. The three mock realizations refer to the cases of catalog galaxies with scrambled Galactic coordinates ($b \rightarrow -b$ and $l \rightarrow -l$) and catalog galaxies randomly distributed (MC (Monte Carlo) label in the plots) over the catalog sky area (see text more details).

Table 2
Significance of the CCF Cross Correlations for Each Energy Bin and Catalog Calculated Using the SFGs1 Model with Free Normalization

CCF	2MASS			SDSS-MG			SDSS-LRG			SDSS-QSO			NVSS (LSS)			NVSS (PSF)		
	χ^2_{bf}	σ	TS	χ^2_{bf}	σ	TS	χ^2_{bf}	σ	TS	χ^2_{bf}	σ	TS	χ^2_{bf}	σ	TS	χ^2_{bf}	σ	TS
$E > 500$ MeV	6.2	3.6	12.9	2.6	2.7	7.4	4.5	0.3	0.1	9.0	4.5	21	30.2	8.0	64.9	3.6	9.9	97.3
$E > 1$ GeV	10.6	4.4	19.4	2.1	3.0	9.3	4.6	0.4	0.2	3.5	2.3	5.1	45.1	8.6	73.6	4.9	10.3	106.4
$E > 10$ GeV	2.0	2.1	4.5	6.2	0.7	0.5	2.6	0.2	0.1	4.8	1.6	2.6	40.4	5.1	25.6	5.8	7.7	59.4

Notes. For each case, the best-fit χ^2_{bf}, the significance σ, and the test statistics TS values are reported. Each fit has nine degrees of freedom (10 bins, 1 free parameter). For the NVSS case, a further model, PSF, is tested.

Table 3
Same as Table 2 but Using CAPS

CAPS	2MASS			SDSS-MG			SDSS-LRG			SDSS-QSO			NVSS (LSS)			NVSS (PSF)		
	χ^2_{bf}	σ	TS	χ^2_{bf}	σ	TS	χ^2_{bf}	σ	TS	χ^2_{bf}	σ	TS	χ^2_{bf}	σ	TS	χ^2_{bf}	σ	TS
$E > 500$ MeV	8.3	3.4	11.5	4.5	3.5	12.1	3.5	0.0	0.0	9.7	5.3	28.6	30.1	8.3	71.3	7.3	9.6	92.3
$E > 1$ GeV	3.7	3.6	12.8	3.9	3.3	11.2	5.4	0.4	0.2	7.6	3.3	10.9	23.1	8.4	70.7	5.3	9.1	82.8
$E > 10$ GeV	5.1	1.6	2.7	8.4	0.7	0.6	4.4	0.7	0.5	4.6	2.7	7.3	21.0	3.4	11.8	9.3	4.8	23.2

overlap significantly with the dN/dz of the DR6 QSOs. The similarity of the model predictions implies that BL Lacs, FSRQs, SFGs, and DR6 QSOs all trace the underlying mass density field at high redshifts.

We note that the SDSS DR6 catalog of QSOs is prone to a systematic error that we did not investigate in the previous sections: contamination by stars. To investigate this issue and assess the magnitude of the effect, we have extracted a large number ($\sim 8 \times 10^4$) of SDSS DR6 stars with apparent magnitudes in the range $16.9 < g < 17.1$ from the CasJobs website. We then estimated the cross correlation between this star catalog and the *Fermi* maps. The resulting CCFs turned out to be consistent with zero, showing that any residual stellar contamination does not correlate with the IGRB and does not contribute to the cross-correlation signal.

7.3. Cross Correlation with 2MASS Galaxies

The 2MASS survey catalog is the most local sample that we have considered. These near-infrared-selected galaxies are likely to trace the local SFG population rather than the AGN population. The results of the analysis are shown in Figure 15. We observe a signal in the CCF at angular separations smaller than $\sim 10^\circ$ with a significance $\sim 3.5\sigma$ and a signal in the CAPS with a similar 3.5σ significance that appears to result mainly from multipoles smaller than ~200. The angular extent and the amplitude of this signature depends on the energy band. Intriguingly, the significance remains stable at $E > 1$ GeV, even slightly increasing, especially in the case of the CCF, possibly indicating a signal peaking at around 1 GeV, as expected for the case of nearby SFGs.

The comparison with the models excludes, with high significance, that BL Lac could give a dominant contribution to the IGRB diffuse emission at low redshift. In this respect, both the CCF and the CAPS provide strong constraints. This result is in agreement with similar independent findings based on the population studies of resolved BL Lacs (Abdo & Ackermann 2010b) and the anisotropy of the IGRB (Cuoco et al. 2012), which both indicate a low-contribution BL Lacs (<20–30%) at least up to ~50 GeV. Above 50 GeV the contribution is more uncertain and can be more significant (Ajello et al. 2014). In this respect, our constraints in the energy range $E > 10$ GeV are weak and do not provide a direct test. Conversely, both SFGs1 and FSRQs are equally good candidates for the IGRB in the energy range explored here. The close match with the data stems from the fact that they have similar $dI(>E)/dz$ at low redshifts. As expected, the predictions for the SFGs2 model are significantly different from the SFGs1 one and do not fit the data. This implies that in model SFGs2 the contribution from SFGs should be <20–30% of the total, as for the BL Lacs. As discussed in Section 2.1, the large differences between the two SFG models originates from the different distributions $dI(>E)/dz$, with the distribution for SFGs2 peaking at very low redshift, as opposed to the SFGs1 one that extends to high redshift. The implications of these differences are discussed in Sections 8 and 9.

7.4. Cross Correlation with NVSS Galaxies

Figure 16 shows the results obtained by cross correlating *Fermi* maps with the NVSS galaxy catalog. In this case we detect a CCF signal with a strong significance of about $\sim 8.0\sigma$ both for $E > 500$ MeV and $E > 1$ GeV on small ($\theta < 1^\circ$) angular scales. In fact, we detect a strong signal also in the highest energy bin ($\sim 5.0\sigma$), though only at $\theta < 0.^\circ 2$. The fact that the peak in the CCF narrows with increasing energy is quite informative and indicates that the signal is intrinsically confined to very small θ, and it extends to larger θ values only because of the spreading-out effect by the LAT PSF, especially at low energies. The width of the peaks $\sim 1.^\circ 5$, $\sim 1.^\circ 0$, and $\sim 0.^\circ 2$ for the CCF at $E > 0.5$, 1, 10 GeV is, indeed, also compatible with the width of the LAT PSFs at these energies. The CAPS gives similar significances and provides additional information on the characteristics and possible origin of the signal. Different from the CAPS with other catalogs, in fact, the CAPS with NVSS is characterized by a strong signal at very high multipoles (up to $l \sim 1000$), confirming that the signal comes mostly from small scales.

All models provide a good match to the data at large ($\theta > 1^\circ$) angular scales. At smaller separations, however, the observed signal overshoots model predictions, especially in the SFGs1 case, as confirmed by the high χ^2_{bf} in Tables 2 and 3. This excess signal correlation on small scales does not seem to be related to the large-scale clustering of astrophysical sources.

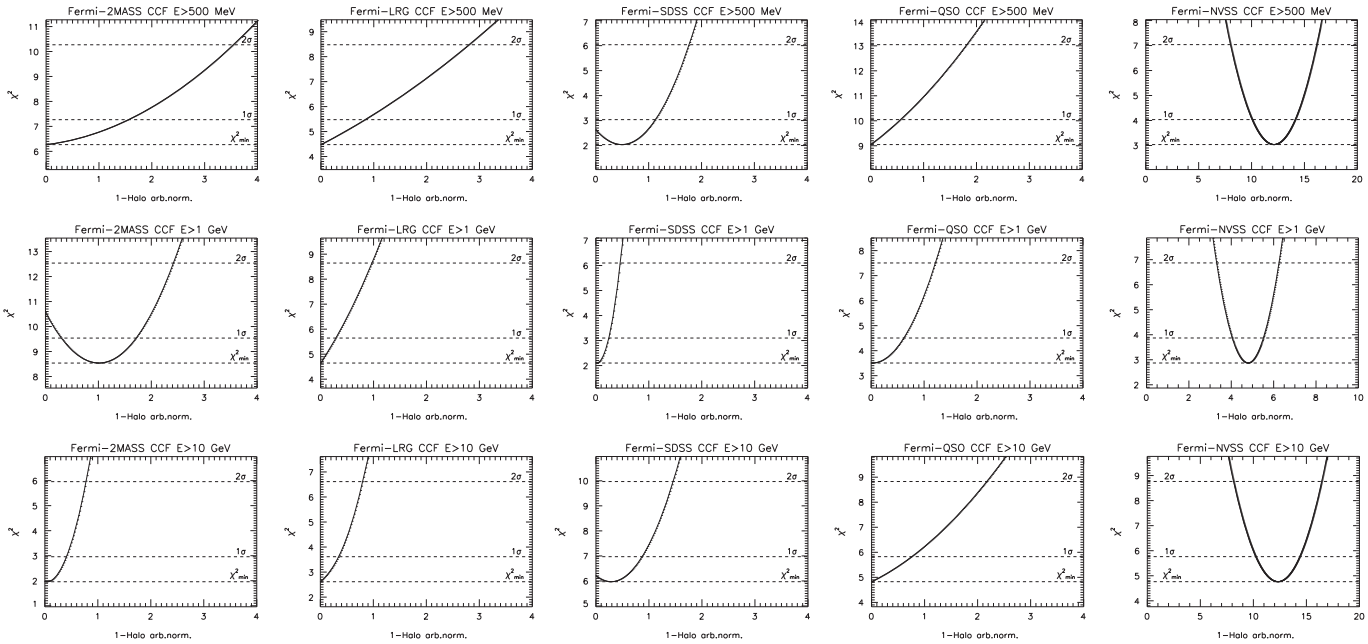

Figure 13. One-dimensional χ^2 profile of the *one-halo*-like normalization (in arbitrary units) from the joint *one-halo*-like and SFGs1 two-dimensional fit. Each panel shows the case of the fit to a single catalog and energy band CCF.

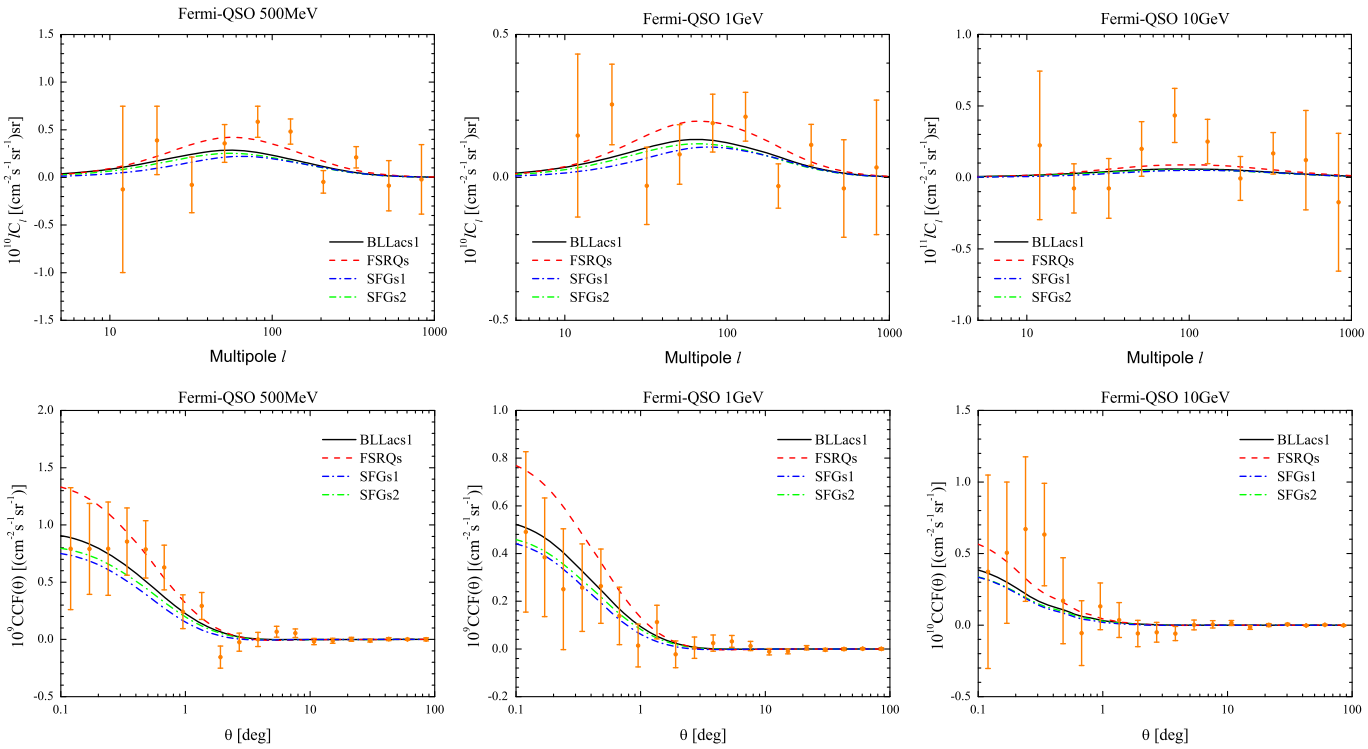

Figure 14. CAPS (upper panels) and CCF (lower panels) estimated from the SDSS DR6 QSOs map and the *Fermi*-LAT IGRB maps in three energy bands. The three panels refer to the three energy cuts $E > 0.5$ GeV (left panels), $E > 1$ GeV (middle panels), and $E > 10$ GeV (right panels). Error bars on the data points (orange dots) represent the diagonal elements of the PolSpice covariance matrix. Model predictions for different types of sources are represented by continuous curves: FSRQs (red, dashed), BL Lacs (black, solid), and star-forming galaxies (blue and green, dot-dashed). All of the models are a priori models (i.e., not fitted), normalized assuming that the given source class contributes 100% of the IGRB.

Instead, this correlation seems to be better described by a *one-halo*-like term. Indeed, as seen in Section 7.1, the NVSS case is the only one where a *one-halo*-like term is strongly detected. Using a *one-halo*-like term as an alternative model to calculate the significance of the signal improves the quality of the fit to both CAPS and CCF, as confirmed by the decrease in the $\chi^2_{\rm bf}$ values and the corresponding increase in statistical significance to $\sim 10.0\sigma$.

It is unclear if this small-scale signal is due to a pure *one-halo* term or to the possibility that a significant fraction of NVSS sources might also be γ-ray emitters. Indeed, the fact that NVSS sources are known to be good candidates for γ-ray

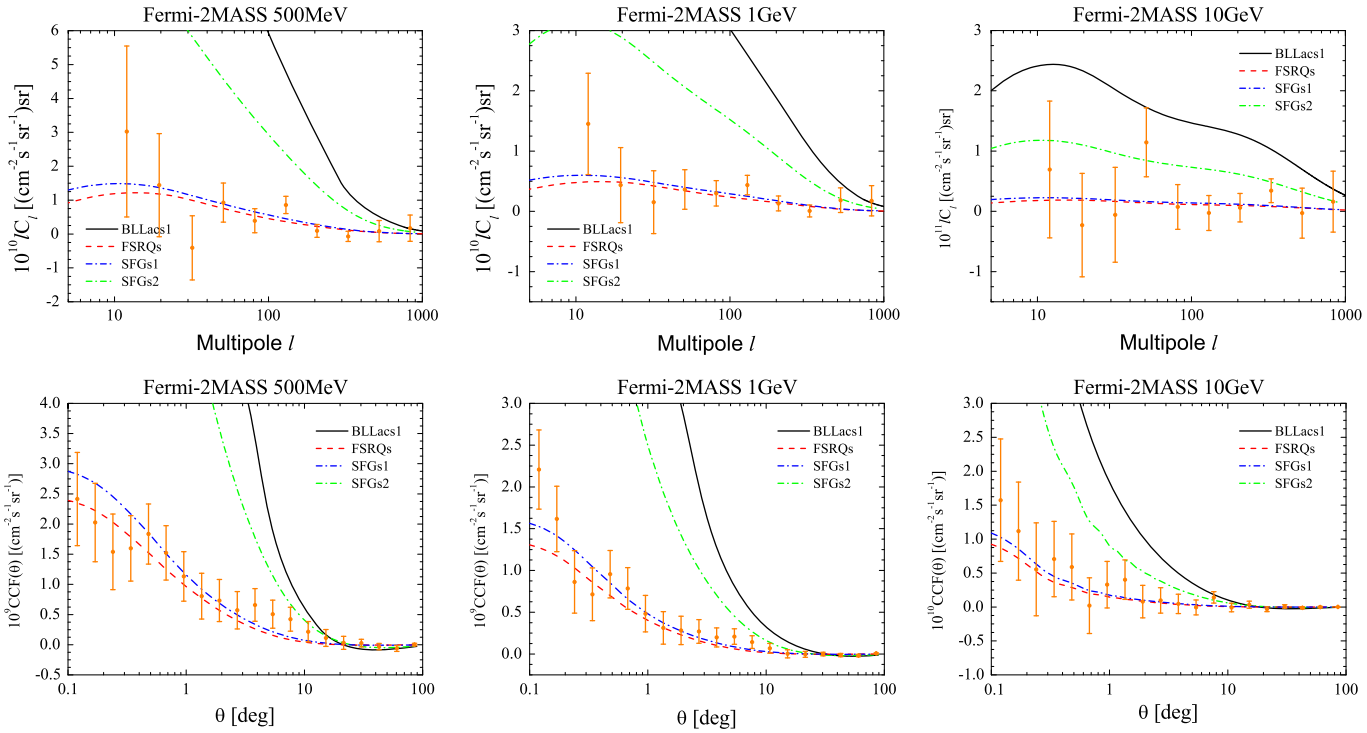

Figure 15. Analogous to Figure 14 using 2MASS galaxies.

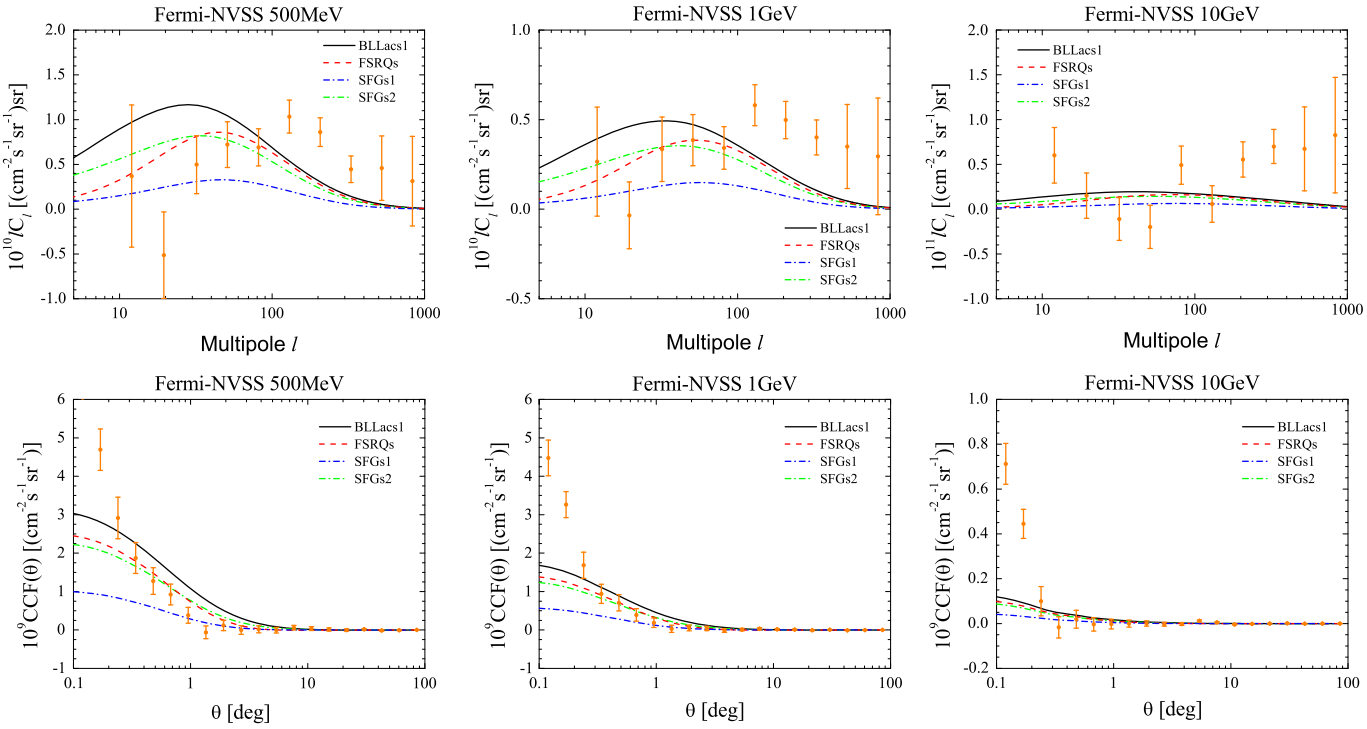

Figure 16. Analogous to Figure 14 using NVSS galaxies.

emission and that this catalog is routinely searched to identify the counterparts of γ-ray sources (Nolan et al. 2012; Acero & Ackermann 2015) is an argument in favor of the second possibility.

A further explanation, possibly not entirely independent of the previous ones, is the presence of duplicate objects in the NVSS catalog. It is well known that a large fraction of close pairs are in fact single objects with a prominent radio jet wrongly classified as a separate, companion object (Overzier et al. 2003). The net result is an excess of pairs at small angular separations that is responsible for an unphysical, large autocorrelation signal at small angles (Overzier et al. 2003), and this could thus induce a corresponding cross-correlation excess.

For all of the above reasons, we adopt a conservative approach and consider the NVSS cross correlation at angles

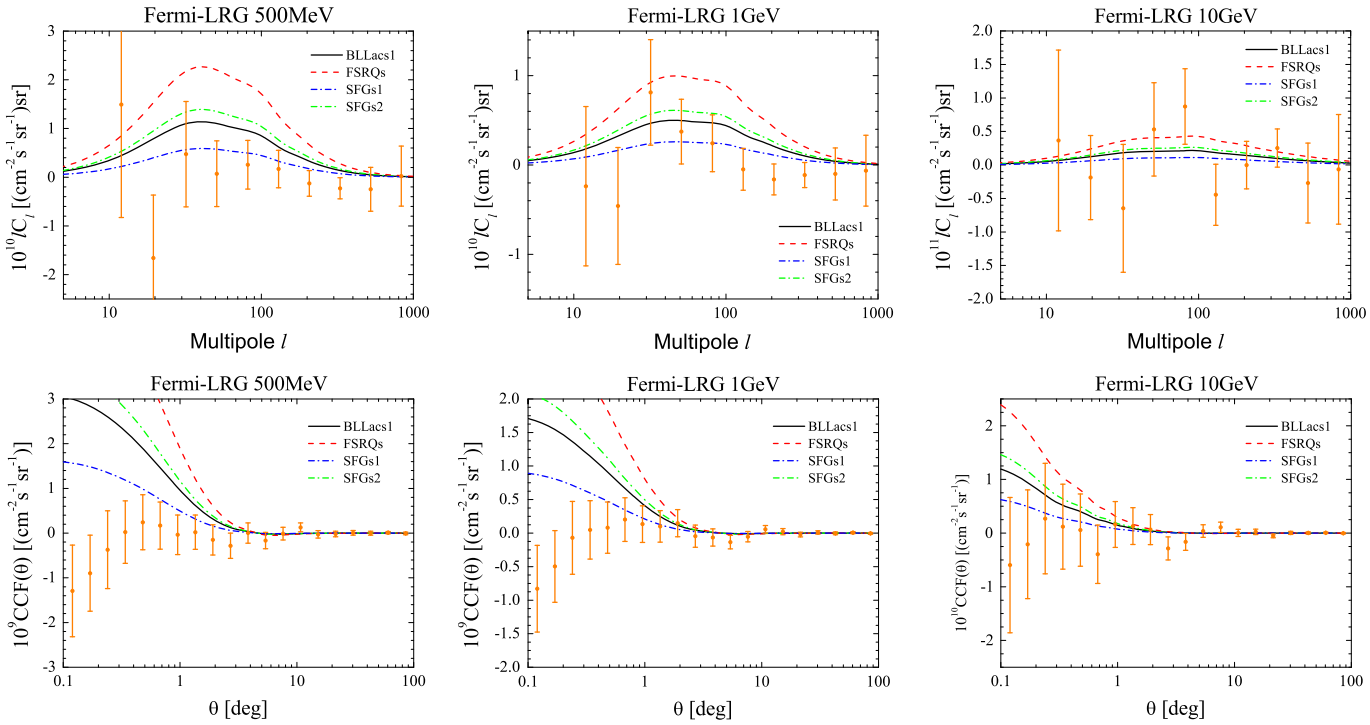

Figure 17. Analogous to Figure 14 using SDSS DR8 luminous red galaxies.

$\theta < 1^\circ$ and multipoles $l > 100$ as arising from physical processes that are not associated with the LSSs, and we will ignore it in the χ^2 analysis performed in the next section.

7.5. Cross Correlation with SDSS DR8 LRGs Galaxies

The results of the cross-correlation analysis between the SDSS DR8 LRGs and the *Fermi*-LAT maps are shown in Figure 17. In this case we do not detect any correlation signal. In fact, the CCF drops below zero at very small angular separations, although the significance of this feature is very weak. A possible reason for this surprising behavior is the aggressive procedure used to remove possible systematics from the raw LRG data (Ho et al. 2012), which might remove the genuine correlation signal along with the spurious one. At larger ($\theta > 0.^\circ 2$) separations, the correlation signal is consistent with zero. This is in agreement with the model predictions for SGFs1 and, to a lesser extent, to BLLacs1 and SFGs2. This is not surprising because the $dI(>E)/dz$ of these sources barely overlap with the narrow dN/dz distribution of the LRGs. On the contrary, the FSRQ model predicts a significant cross correlation, which is at variance with the data.

7.6. Cross Correlation with SDSS DR8 Main Galaxy Sample

In Figure 18 we plot the estimated CAPS and CCF between the *Fermi*-LAT maps and the SDSS DR8 galaxies in the main sample. We observe a correlation signal at small angles at about the $\gtrsim 3\sigma$ level for both the $E > 500$ MeV and the $E > 1$ GeV cases, similar to the 2MASS case. The observed CCF is marginally consistent for $E > 1$ GeV, with theoretical predictions if the sources of the IGRB are SFGs in model SFGs1. In all AGN-based models the predicted cross-correlation signal is much higher than the observed one. This is similar to the 2MASS case except that the dN/dz of the DR8 galaxies peak at significantly higher redshift than the 2MASS galaxies. We conclude that in this case SFGs provide a significant contribution to the IGRB not only locally but also at $z \sim 0.3$ and that their contribution is more important than that of BL Lacs and FSRQs. In the case of the SFGs2 model, instead, SFGs are predicted to have a small contribution, similar to the one of blazars.

8. χ^2 ANALYSIS

To quantify the qualitative conclusions drawn from the inspection of the correlation analysis performed in the previous section, we now perform a χ^2 comparison between the model predictions discussed in Section 2 and the CCF and CAPS estimates presented in Section 7. The aim is to estimate the free parameters of the models, i.e., to quantify the relative contribution of different types of potential sources to the IGRB and to assess the goodness of the fit, from which we can infer what is the most likely mix of source candidates responsible for the observed IGRB. Here we present only the results of the CCF analysis because those obtained with the CAPS are fully consistent with those shown below.

For each CCF estimated by comparing a galaxy catalog and a *Fermi*-LAT map above a given energy threshold, we compute the following χ^2 statistics:

$$\chi^2 = \sum_{ij} \big(d_i - m_i(\alpha)\big) C^{-1}_{\theta_i\theta_j} \big(d_j - m_j(\alpha)\big), \qquad (28)$$

where $C_{\theta_i\theta_j}$ is the covariance matrix computed using PolSpice that quantifies the covariance among different angular bins θ_i, d_i represents the data, i.e., the CCF measured at the angular bin i, and $m_i(\alpha)$ is the model prediction that depends on a set of parameters α. We note that it is important to use the full covariance matrix because the different bins are significantly correlated, a feature which is typical of CCF measurements.

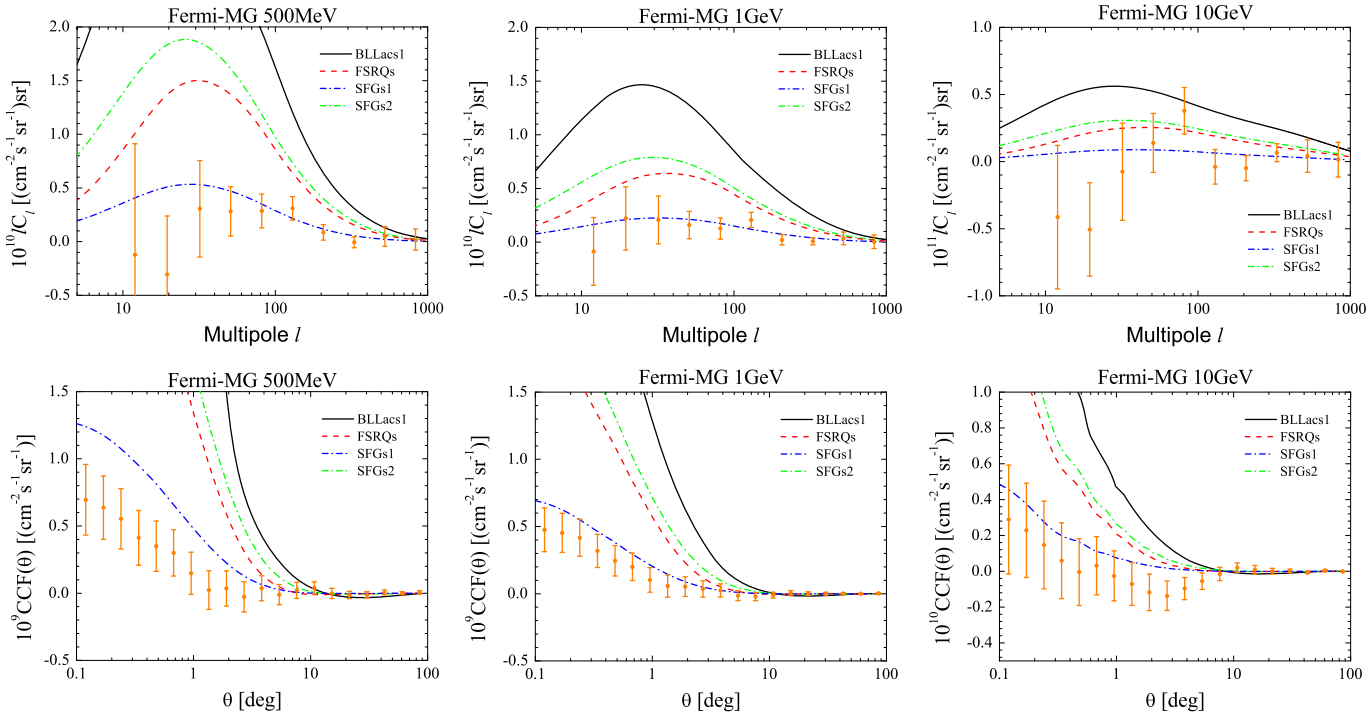

Figure 18. Analogous to Figure 14 using SDSS DR8 Main Galaxy Sample.

Instead, the covariance matrix of the CAPS is to a better approximation diagonal (although some sizable correlations are nonetheless present, in particular for low and high multipoles), at the price, however, of making the interpretation less intuitive because it lacks the immediate identification of the scale(s) responsible for the correlation, which is instead present for the analysis in real space with the CCFs. Thanks to the fact that we are considering γ-ray flux maps rather than fluctuation maps, we can express the model CCF as a sum of different contributions corresponding to the CCF of different source types: $m_i = f_{\rm sfg}\ c_{\rm sfg}(\theta_i) + f_{\rm bllac}\ c_{\rm bllac}(\theta_i) + f_{\rm fsrq}\ c_{\rm fsrq}(\theta_i)$, where $c_\alpha\ (\theta_i)$ is the model CCF for a given type of source when it represents 100% of the IGRB, and f_α is a free parameter that quantifies the actual IGRB fraction contributed by the source. Note that, in our analysis, we do not require that $\sum f_\alpha = 1$. Instead we verify that this condition is verified a posteriori.

In Equation (28) the sum extends over 10 angular bins logarithmically spaced between $\theta = 0.^\circ 1$ and 100°. We use logarithmic bins to emphasize small scales where the signal-to-noise ratio is higher, whereas the choice of 10 bins is dictated by the compromise between the need to robustly invert the covariance matrix (an operation that becomes unstable when too many correlated bins are considered) and to maximize the available information. The number of bins used in the χ^2 analysis (10) is smaller than that used in the CCF plots shown in the previous section (20), in which the aim was to illustrate the qualitative agreement between models and data.

The total χ^2 accounts for the contributions from the CCF of all catalogs. The only exception is the CCF of NVSS sources, for which we have ignored separations $\theta < 1^\circ$ because, as discussed in the previous section, the signal in that range is likely not related to LSS clustering. In particular, the total χ^2 for the $E > 500$ MeV band is the quantity that we use to perform the bulk of the analysis detailed below. However, we have also considered the cases in which the χ^2 only accounts for the CCF of a subset of catalogs or of different energy bands. Investigating the contribution to χ^2 by different catalogs is important to illustrate the tomographic nature of our analysis. On the contrary, considering different energy cuts turns out to be not very revealing. In principle, breaking out the total χ^2 by energy bands provides additional information to identify the contribution to the IGRB by different sources. However, the constraints derived from the two higher energy bands are weak, and the χ^2 discriminating power is dominated by the $E > 500$ MeV band. The practical outcome is that the results obtained by considering photons with $E > 1$ GeV or $E > 10$ GeV are fully consistent with those obtained with the $E > 500$ MeV energy band.

We have performed our χ^2 analysis in three steps in which we increase the complexity of the IGRB model: (1) the one-source scenario, in which we assume that only one type of source, FSRQs, BL Lacs, or SFGs, contributes to the IGRB, (2) the two-source scenario, in which we allow for two possible contributors to the IGRB, and (3) the three-source scenario in which FSRQs, BL Lacs, and SFGs can contribute to the diffuse background. As we already noted, in all three cases the overall normalization is free: we do not impose that the overall contribution should sum up to or not exceed the observed IGRB. Instead we have checked that, after minimizing the χ^2, this condition is satisfied in all cases explored.

The results of the χ^2 minimization are summarized in Table 4 for the one-source (upper part), two-source (middle section), and three-source (bottom) scenarios. In the table we list the minimum χ^2 value with the three best-fit parameters in parentheses, i.e., the IGRB fraction contributed by SFGs, BL Lacs, and FSRQs, respectively. In the one- and two-source scenarios, the values of the sources not considered in the fit are set equal to zero, and the related space in the table is left blank for clarity. The two columns refer to the two different BL Lac

Table 4
Minimum χ^2 for the One-, Two-, and Three-Source Models and Best-Fit Values for the Free Parameters Corresponding to the Fraction of the IGRB Contributed by SFGs, BL Lacs, and FSRQs

	BLLacs1				BLLacs2			
	χ^2	$f_{\rm SFGs}$	$f_{\rm BLLs}$	$f_{\rm FSRQs}$	χ^2	$f_{\rm SFGs}$	$f_{\rm BLLs}$	$f_{\rm FSRQs}$
SFGs1	35.3	0.72	⋯	⋯	35.3	0.72	⋯	⋯
BLLacs	44.3	⋯	0.08	⋯	43.1	⋯	0.18	⋯
FSRQs	48.8	⋯	⋯	0.24	48.8	⋯	⋯	0.24
SFG1s + BLLacs	35.3	0.72	0.0	⋯	35.3	0.72	0.0	⋯
FSRQs + SFGs1	35.3	0.72	⋯	0.0	35.3	0.72	⋯	0.0
FSRQs + BLLacs	42.0	⋯	0.06	0.10	43.1	⋯	0.18	0.0
FSRQs + BLLacs + SFGs1	35.3	0.72	0.0	0.0	35.3	0.72	0.0	0.0
FSRQs + BLLacs + SFGs2	41.7	0.14	0.0	0.12	41.7	0.14	0.0	0.06

Table 5
Contribution to the Best-fit χ^2 from the Single Catalog CCFs with the $E > 500$ MeV γ-Ray Map for the Two Models FSRQs + BLLacs1 + SFGs1 and FSRQs + BLLacs1 + SFGs2

	2MASS (10)	NVSS (6)	SDSS-MG (10)	SDSS-LRG (10)	SDSS-QSO (10)
FSRQs + BLLacs1 + SFGs1	6.4	1.5	3.6	7.7	16.1
FSRQs + BLLacs1 + SFGs2	6.2	1.5	3.1	6.6	24.3

Note. The numbers in parentheses are the number of θ bins used to calculate the χ^2.

models that we have considered (BLLacs1 and BLLacs2). Note that we quote total χ^2 values rather than reduced ones because it is not straightforward to calculate the number of degrees of freedom involved. This quantity, in fact, is not simply equal to the number of bins over which the χ^2 is calculated due to the presence of correlation among different catalogs, because their redshift distributions and angular coverages overlap significantly. Instead, to assess the goodness of fit, we quote, for the case of the three-parameter models, the best-fit χ^2 values for the cross correlation between each single catalog and the *Fermi* $E > 500$ MeV map. These χ^2 values are presented in Table 5, which can be compared with the number of degrees of freedom, given approximately by the number of bins used minus the number of fit parameters. The results indicate that the fit to each catalog for the three-parameter models is adequate, except for a tension with the QSO CCF in the SFGs1 model that is even more prominent in the SFGs2 model. The tension among the models results in the underprediction of the observed correlation.

The main results of the χ^2 analysis are as follows.

1. All models that include a contribution from SFGs provide a significantly better fit than those in which the IGRB is contributed to by AGNs only.
2. Model SFGs1 performs better than SFGs2. The main issue with the SFGs2 model is that it provides a poor fit to the CCF of the SDSS QSOs, as indicated in Table 5, whereas for all other data sets the two SFG models fit the data equally well, although with different overall normalizations of the SFG signal.
3. In all models explored, the IGRB contribution from AGNs is subdominant. When SFGs are included among the IGRB sources, the AGN contribution is consistent with zero. The consistency with zero simply reflects the limited accuracy of our analysis, which does not account for the fact that, based on the observed number count distribution of the resolved γ-ray sources, some contribution from AGNs is to be expected (Ajello et al. 2012, 2014).
4. The BLLacs1 and BLLacs2 models have similar χ^2 values, although the normalization of the BLLacs two-component model is approximately a factor of two higher than the BLLacs1 model.

The uncertainties in the estimates of the parameters can be appreciated from the sets of panels shown in Figures 19 (SFGs1 model) and 20 (SFGs2 model). We do not show results for the BLLacs2 case because they are very similar to those of the BLLacs1 case when one rescales the BL Lac component by a factor of ∼2. Among the plots, those with the one-dimensional χ^2 represent the contribution to the IGRB from a specific type of source that we obtain by *profiling* (Rolke et al. 2005) over the other contributors. For example, in the case of SFGs, this is the function obtained after minimizing the $\chi^2(f_{\rm sfg}, f_{\rm bllac}, f_{\rm fsrq})$ with respect to $f_{\rm bllac}$ and $f_{\rm fsrq}$. The plots show the χ^2 together with the 2σ significance level. The plot in the upper-right corner also shows the derived quantity $f_{\rm tot}$, i.e., the total IGRB fraction, $f_{\rm tot} = f_{\rm sfg} + f_{\rm bllac} + f_{\rm fsrq}$. The two-dimensional contours refer to the function obtained by profiling over only one parameter. In this case, the contours are drawn in correspondence to the 1, 2, and 3σ confidence levels. The constraints on the SFGs are rather broad: they show that, within 2σ, the contribution to the IGRB of these sources varies in the range 25–95%. The constraints are tighter in the case of the BLLacs2 model (50–95%), not shown in the plots. A scenario with no SFG contribution is rejected with high statistical significance. The contribution of AGNs is consistent with zero but, within 2σ, can be as large as 5–7% and 7–8% for the FSRQs and BL Lacs, respectively.

For the SGFs2 model, which provides a worse fit than SFGs1, we only obtain upper limits: the SFG contributes $\leqslant$20% to the IGRB, and the contributions of BLLacs1 and FSRQs are

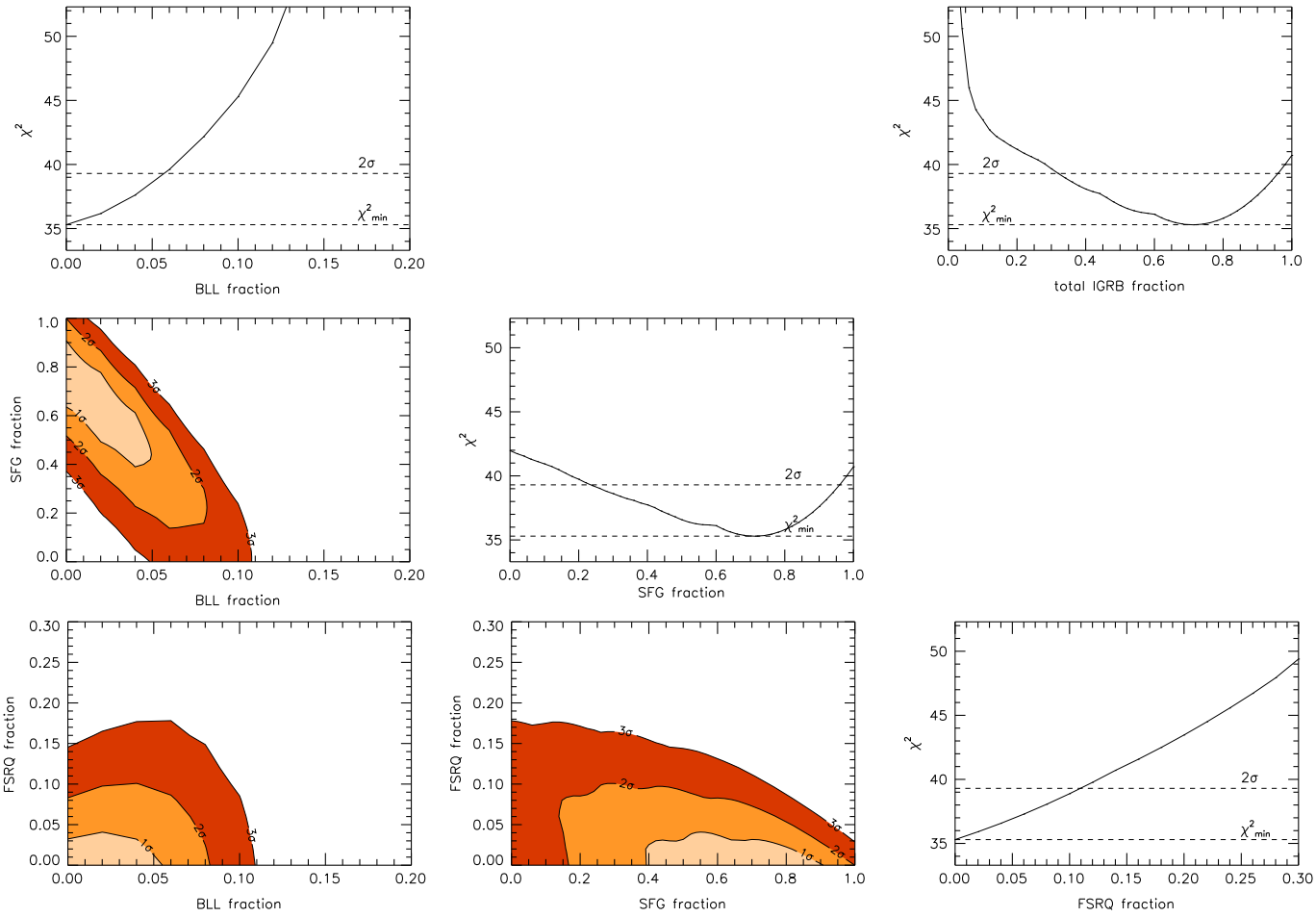

Figure 19. Plot matrix showing the one-dimensional profile likelihoods for each component and contours of the two-dimensional profile likelihoods for the three-component fit (BL Lacs, FSRQs, and SFGs) to all of the experimental CCFs (i.e., all catalogs and all energy ranges). The plots refer to the models BLLacs1 and SFGs1. The plot in the upper-right corner shows the profile likelihood for the total IGRB fraction.

limited to 10% and 20%, respectively. Note that in this case the contribution from FSRQs is larger than in the SFGs1 model. Another difference between models SFGs1 and SFGs2 is the total contribution to the IGRB. The three-source model SFGs1 +BLLacs1+FSRQs is able to account for a large fraction of the IGRB, about 70–80%, whereas the model SFGs2+BLLacs1 +FSRQs can only be responsible for ∼20–30% of the IGRB. Table 5 emphasizes the main issue with the model SFG2 +BLLacs1+FSRQs, which is the poor fit to the QSO CCF. Indeed, visual inspection of the CCF confirms that this model cannot explain the amplitude of the measured cross-correlation signal. Instead, model SFGs1+BLLacs1+FSRQs provides a better fit to the data, apart from a small residual underestimate of the QSO correlation signal.

Finally, another interesting feature of the two-dimensional χ^2 contours is the nonnegligible correlation among the contributing fractions. The fact that these contours are not completely degenerate, however, is a nontrivial result that we have obtained by cross correlating the *Fermi* maps with different catalogs of objects spanning different redshift ranges or, in other words, to the tomographic nature of our χ^2 analysis. To illustrate this point, let us consider the simple two-source model BLLacs2+SFGs1 instead of the three-source one BLLacs2+SFGs1+FSRQs. The advantage is that in this case the two-dimensional function $\chi^2(f_{\rm sfg}, f_{\rm bllac})$ encodes all information that, instead, is partially lost when one profiles the three-source model. We show in Figure 21 the 1 and 2σ contours of the SFG+BL Lac contributions superimposed on the 1 and 2σ contours obtained when only one type of catalog is considered. Here we show the χ^2 values obtained by cross correlating the *Fermi* maps with SDSS QSOs, SDSS galaxies, and 2MASS galaxies. Individual constraints are fully degenerate because one can only constrain the ratio of the two contributions. In particular, constraints from objects at low redshifts, like 2MASS and SDSS galaxies, would only narrow the width of the uncertainty strip without removing the degeneracy. It is only when we consider SDSS QSOs that convey information on clustering at high redshifts that we are able to remove part of the degeneracy. Note that the combined constraints are consistent with those obtained from the analyses of the individual catalogs.

9. DISCUSSION AND CONCLUSIONS

In this work we have cross correlated the *Fermi*-LAT sky maps obtained in 60 months of observations with the angular positions of several types of extragalactic objects at different redshifts. The aim is to constrain the origin of the IGRB under the hypothesis that it is constituted by unresolved astrophysical sources that can be traced by but do not necessarily coincide with the objects in the catalogs. The benefit of performing a

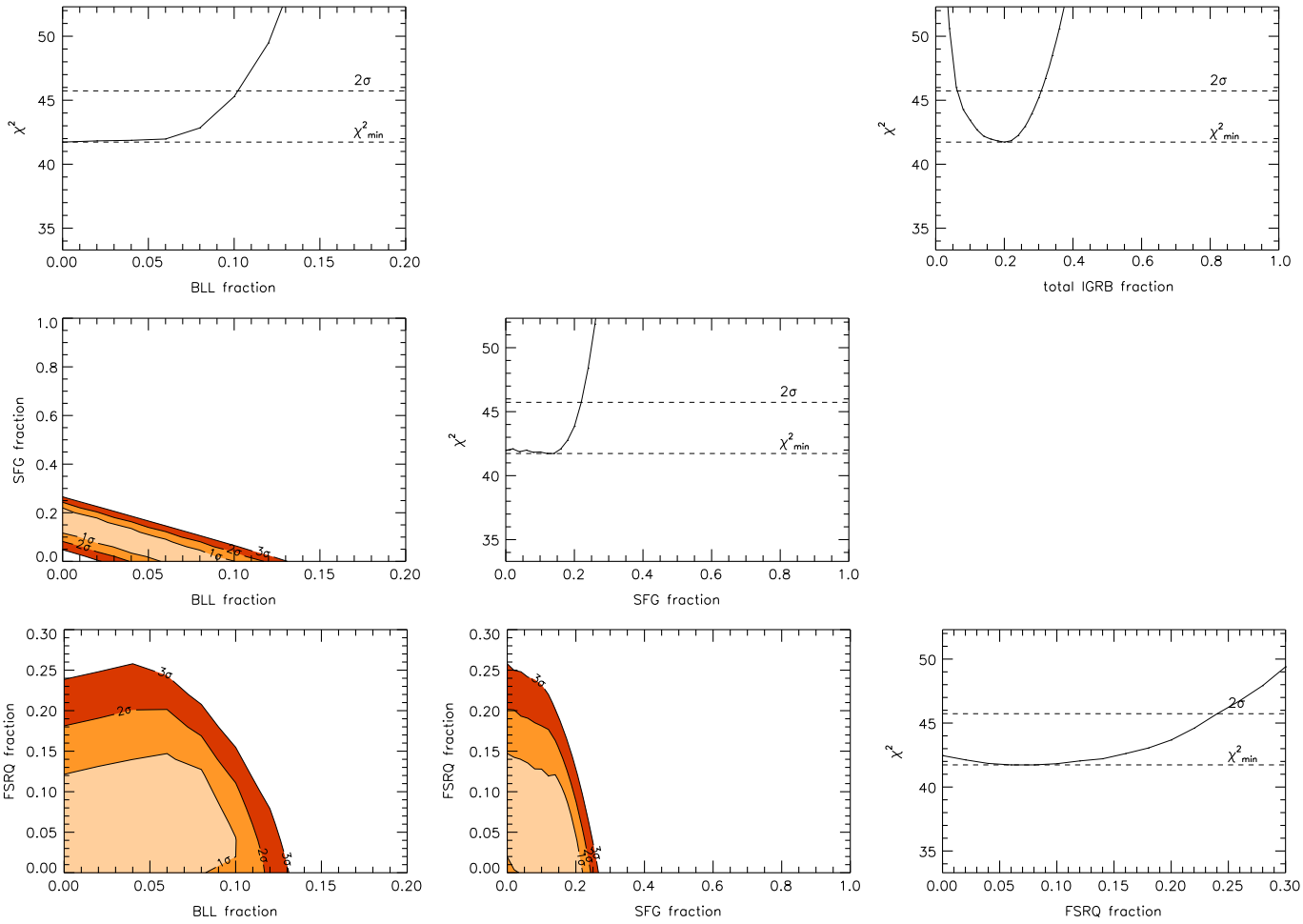

Figure 20. Same as Figure 19 but for models BLLacs1 and SFGs2.

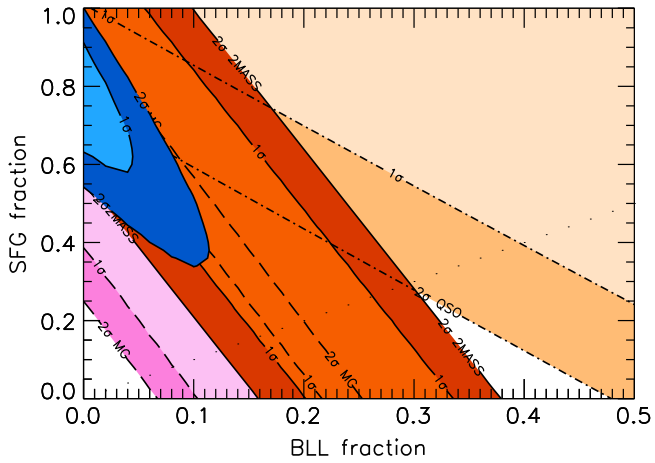

Figure 21. χ^2 contours for the two-component model SFG+BLLacs2 with respect to the three subsets of CCFs with the SDSS QSOs (pale brown, dot-dashed), the 2MASS (red, solid), and the SDSS MG (pink, dashed) catalogs, and the combined data set (blue, solid). The complementary tomographic information from the different catalogs helps to break the degeneracies present when using a single catalog.

cross-correlation analysis of the IGRB rather than considering its mean amplitude or its autocorrelation properties is that the cross correlation is less prone to systematic effects that may arise from the inaccurate cleaning of the γ-ray maps, such as imperfect subtractions of the diffuse Galactic foreground and contributions from charged particles.

For this purpose we rely on two complementary statistical tools: the angular two-point correlation function and its Legendre transform, the angular power spectrum. The results of our cross-correlation analysis were compared with theoretical predictions in which one assumes that the IGRB is constituted, in full or in part, by any of these potential candidates: SFGs, BL Lacs, and FSRQs.

The main results of our analysis are as follows.

1. We observe a significant (>3–4σ) signal in the angular CCF of 2MASS galaxies, NVSS galaxies, and QSOs with the IGRB on scales smaller than 1°. A weaker signal, $\sim$3 σ, is also observed for SDSS Main Sample galaxies. Whereas in the case of 2MASS the cross-correlation signal is observed in all energy bands and seems to be genuinely related to the underlying clustering properties of matter, in the case of NVSS we interpret the CCF signature as not originating from the LSSs. The NVSS signature is likely attributed, at least in part, to undetected γ-ray sources that have counterparts in the NVSS catalog and to spurious close pairs in the catalog that are, in fact, a single object. The fact that a cross-correlation signal on small scales is also observed when we consider SDSS galaxies and SDSS QSOs is a very interesting result

because it suggests that the CCF signal does not solely originate at redshift $z \lesssim 0.1$, where 2MASS and SDSS galaxies are found, but is also contributed to by high-redshift ($z > 1$) clustering that is traced by the QSOs in the SDSS catalog.

2. The fact that we now observe a signal in several cross-correlation analyses is beyond the original expectations of Xia et al. (2011), who performed an analysis similar to the one presented here using *Fermi*-LAT two-year maps. Their forecast, however, was based on the assumptions that errors were dominated by Poisson noise from discrete photon counts. Our positive result relies on several improvements that have enabled us to efficiently remove potential sources of systematic and random errors. In particular, (1) in the map cleaning procedure we have used three different models for the Galactic diffuse foreground that update and improve the one used in the original analysis, (2) we were able to excise a larger number of individually resolved sources from the γ-ray maps thanks to the most recent LAT source catalogs, (3) we added another set of discrete sources, the SDSS Main Galaxy catalog, in our cross-correlation analyses, and (4) the PSF of the LAT was better characterized. The latter improvement is probably the most crucial because it not only allows us a better comparison between model and data, but it also allows us to push our analysis down to 500 MeV, significantly increasing the photon statistics and reducing the amplitude of statistical errors, and to smaller angular scales than Xia et al. (2011), below 1°, where the signal is the most prominent.
3. We have verified with a series of dedicated tests that the results of our cross-correlation analysis are robust to (1) the cleaning procedure of the *Fermi* maps, (2) the subtraction of the Galactic diffuse foreground, (3) the removal of the resolved γ-ray sources, (4) the choice of the mask, (5) the γ-ray conversion layer in the LAT, (6) the statistical estimator used to measure the angular CCF, and (7) the method adopted to assess the uncertainties in the CCF and CAPS and their covariance. In addition, we have verified that our characterization and treatment of the PSF of the telescope is good and does not introduce any significant systematic error in the comparison between models and data.
4. The comparison between measured cross-correlation signals and model predictions indicates that the best fit to the data is obtained when SFGs are the main, if not the only, contributors to the IGRB (possibly degenerate with MAGNs; see below) and AGNs provide a minor, possibly negligible, contribution. We have explored different combinations of sources and different models for the γ-ray contribution from BL Lacs and SFGs. Models that include SFGs outperform those that consider AGNs only. And among the SFG models explored, the one proposed by Fields et al. (2010) that includes the effect of gas quenching and its redshift dependence provides a better fit to the data than the one proposed by Tamborra et al. (2014), which, instead, ignores this effect.

   Our χ^2 analysis makes these statements more quantitative and shows that, for the model that provides the best fit, SFGs contribute to 72^{+23}_{-37}% (but see our discussion of MAGNs below) of the IGRB (2σ confidence interval), whereas BL Lac and FSRQs provide similar contributions ranging from zero to 8% each. In none of our best-fit models does the contribution to the IGRB total up to 100%. This is an interesting result that keeps open the possibility that other types of sources could contribute to the γ-ray background. In the framework of the cross-correlation analysis one can only speculate on the nature of these sources. Among the different options, the possibility that they consist of astrophysical sources at high redshifts, that would not be detected by our cross-correlation analysis, or that they originate from the annihilation or decay of dark matter particles, is especially intriguing and will be investigated in future analyses.
5. Model predictions depend on a number of parameters, including the bias relation of the mass tracer. Current models of galaxy evolution do not provide reliable predictions for the bias of BL Lacs, FSRQs, and SFGs, which are only weakly constrained by observations. For this reason we run a series of robustness tests in which we have considered the alternative bias models described in Section 2.1.

   For BL Lacs and FSRQs, we have considered the case of constant bias $b_{\rm FSRQ} = b_{\rm BLLac} = 1.04$ as well as that of a z-dependent bias matching that of a $10^{13}\,M_\odot$ dark matter halo. The first scenario predicts a larger cross-correlation signal for low-redshift objects (i.e., 2MASS and SDSS galaxies) than in the reference case. It is a ~20% effect that improves the match between the FSRQ model and data. At higher redshift the cross correlation slightly decreases. However, the effect is very small and does not affect the outcome of the model versus data comparison. In the second scenario, the bias is systematically larger than the reference one at all redshifts, significantly increasing the amplitude of the predicted cross correlation. The net result is that, in this rather extreme case, our conclusion that SFGs contribute to the bulk of the IGRB still holds. The major change is that the predicted contributions from BL Lacs and FSRQs are unlikely to differ from zero.

   For the SFGs we have considered an alternative model in which the bias is set equal to that of a $10^{12}\,M_\odot$ dark matter halo. The bias of this object is larger than the reference value $b_{\rm SFG} = 1$ at all redshifts. As a result, the amplitude of the cross-correlation signal is expected to increase. However, the fractional increase is very small (<10%), and, because of the large error bars of the observed cross-correlation data points, this change does not significantly affect our main conclusion that the IGRB is mainly produced by the SFGs.
6. Our results seem to be consistent, within the uncertainties, with the outcome of different, independent analyses. Ajello et al. (2014) have been able to estimate the contribution of unresolved BL Lacs to the IGRB from their γ-ray LF measured from LAT data and found that they do not account for more than 10–15% of the IGRB signal, consistent with our results. In similar analyses focused on the FSRQs, Dermer (2007), Inoue & Totani (2009), Inoue et al. (2010), and Ajello et al. (2012) have found that these objects provide a similar contribution (~10%) to the IGRB, again in agreement with our results, possibly increasing to ~20% when one accounts for

objects with misaligned jets.

As for SFGs, the estimate of Ackermann et al. (2012a) of a 4–23% contribution to the IGRB is consistent with our estimate of 20–95%, which, although it favors a higher value, has a large uncertainty. A larger contribution from SFGs has also been recently suggested by Tamborra et al. (2014), which might be due to accounting for SFGs at $z > 2$ in the IR LF that have been recently observed by Herschel PEP/HerMES (Gruppioni et al. 2013).

It is also worth noticing that, within the 2σ error bar, our results are also consistent with those of Fields et al. (2010) that, based on the extrapolation of the γ-ray production in the MW, find that SFGs contribute to $\sim$50 % of the IGRB (with rather large uncertainties).

7. In our analysis we have ignored MAGNs, even if they are likely to contribute to the IGRB and its fluctuations, and we restricted our modeling to SFGs and blazars. This is because the expected cross-correlation signal from these sources is robust to uncertainties in their bias parameters, whereas in the MAGNs case model, the predictions are much more sensitive to both their contribution to IGRB at high redshift and their (large) bias. Indeed, we find that, within the current uncertainties, their contribution to CCF and CAPS is degenerate with that of SFGs. One should keep this in mind when interpreting the results of our cross-correlation analysis. It might underestimate the expected cross-correlation signal at high redshift and, consequently, overestimate the SFG contribution, whereas, in fact, part of the observed cross correlation may be due to MAGNs. Possible ways to isolate the contribution of MAGNs are more stringent observational or theoretical constraints on their bias and cross-correlation analyses with catalogs of high redshift objects.

The results of our work indicate possible directions for future research. Our analysis, which is mostly sensitive to sources at $z < 2$, suggests that the combined emission from SFGs, BL Lacs, and FSRQs within this redshift does not completely account for the whole diffuse IGRB signal. Extending our cross-correlation analysis to higher redshifts and using deeper catalogs of extragalactic sources can provide further information to clarify this scenario.

While we observe a significant cross-correlation signal, the amplitude of the errors is still too large to efficiently discriminate among alternative IGRB models. We have learned that *Fermi* IGRB maps improve in both accuracy and precision with time, not only because of the better photon statistics but also thanks to the revised Galactic diffuse model, better characterization of the LAT PSF, and the identification and subtraction of an increasing number of point sources. We therefore expect that errors will be further reduced with the next *Fermi* data releases. Major improvements are also expected from multiwavelength catalogs because the next few years will see the advent of next-generation galaxy redshift catalogs like eBOSS,[21] DESI (Schlegel et al. 2011), and Euclid (Laureijs et al. 2011), extending over a large faction of the sky and containing tens of millions to billions of objects with spectroscopic or photometric redshifts. With these future surveys, we not only expect to reduce the uncertainties in the cross-correlation analysis but also to be able to fully exploit their tomographic potential, which we have only started exploring in this work.

[21] http://www.sdss3.org/future/

J.X. is supported by the National Youth Thousand Talents Program, the National Science Foundation of China under grant No. 11422323, and the Strategic Priority Research Program "The Emergence of Cosmological Structures" of the Chinese Academy of Sciences, grant No. XDB09000000. E.B. and M.V. are supported by INFN-PD51 INDARK. M.V. is supported by FP7 ERC starting grant "cosmoIGM" and by PRIN INAF "A complete view on the first two billion years of galaxy formation" and PRIN MIUR. E.B. acknowledges the financial support provided by MIUR PRIN 2011 "The dark Universe and the cosmic evolution of baryons: from current surveys to Euclid" and Agenzia Spaziale Italiana for financial support from the agreement ASI/INAF/I/023/12/0. The work of A.C. is supported by the research grant *Theoretical Astroparticle Physics* number 2012CPPYP7 under the program PRIN 2012 funded by the Ministero dell'Istruzione, Università e della Ricerca (MIUR), by the research grant *TAsP (Theoretical Astroparticle Physics)* funded by the Istituto Nazionale di Fisica Nucleare (INFN). We wish to thank Keith Bechtol, Seth Digel, Luca Latronico, Philippe Bruel, Nicola Omodei, Eric Charles, Luca Baldini, and Massimo Persic for a careful reading of the manuscript and for providing useful comments.

The *Fermi*-LAT Collaboration acknowledges generous ongoing support from a number of agencies and institutes that have supported both the development and the operation of the LAT as well as scientific data analysis. These include the National Aeronautics and Space Administration and the Department of Energy in the United States, the Commissariat à l'Energie Atomique and the Centre National de la Recherche Scientifique/Institut National de Physique Nucléaire et de Physique des Particules in France, the Agenzia Spaziale Italiana and the Istituto Nazionale di Fisica Nucleare in Italy, the Ministry of Education, Culture, Sports, Science and Technology (MEXT), High Energy Accelerator Research Organization (KEK), and Japan Aerospace Exploration Agency (JAXA) in Japan, and the K.A. Wallenberg Foundation, the Swedish Research Council, and the Swedish National Space Board in Sweden.

Additional support for science analysis during the operations phase is gratefully acknowledged from the Istituto Nazionale di Astrofisica in Italy and the Centre National d'Études Spatiales in France.

Some of the results in this paper have been derived using the HEALPix (Górski et al. 2005) package.

REFERENCES

Abdalla, F. B., Banerji, M., Lahav, O., & Rashkov, V. 2008, arXiv:0812.3831
Abdo, A., Ackermann, M., Ajello, M., et al. 2011, ApJ, 734, 116
Abdo, A. A., Ackermann, M., Ajello, M., et al. 2010a, PhRvL, 104, 101101
Abdo, A. A., Ackermann, M., Ajello, M., et al. 2010b, ApJ, 720, 435
Abdo, A. A., Ackermann, M., Ajello, M., et al. 2012, ApJ, 758, 140
Abdo, A. A., Ackermann, M., Atwood, W. B., et al. 2015, ApJS, submitted
Ackermann, M., Johannesson, G., Digel, S., et al. 2009, in AIP Conf. Proc. 4th International Meeting on High Energy, Gamma-Ray Astronomy 1085 ed. F. A. Aharonian, W. Hofmann, & F. Rieger (Heidelberg: AIP), 763
Ackermann, M., Ajello, M., Albert, A., et al. 2012a, PhRvD, 85, 083007
Ackermann, M., Ajello, M., Atwood, W. B., et al. 2012b, ApJ, 750, 3
Ackermann, M., Ajello, M., Allafort, A., et al. 2012a, ApJ, 755, 164
Ackermann, M., Ajello, M., Albert, A., et al. 2012b, ApJS, 203, 4
Ackermann, M., Ajello, M., Allafort, A., et al. 2013, ApJ, 765, 54

Ackermann, M., Ajello, M., Albert, A., et al. 2014a, ApJ, 799, 86
Ackermann, M., Albert, A., Albert, A., et al. 2014c, ApJ, 793, 64
Afshordi, N., Loh, Y., & Strauss, M. A. 2004, PhRvD, 69, 083524
Aihara, H., Allende Prieto, C., An, D., et al. 2011, ApJS, 193, 29
Ajello, M., Shaw, M. S., Romani, R. W., et al. 2012, ApJ, 751, 108
Ajello, M., Romani, R. W., Gasparrini, D., et al. 2014, ApJ, 780, 73
Ando, S. 2014, arXiv:1407.8502
Ando, S., & Komatsu, E. 2013, PhRvD, 87, 123539
Ando, S., Komatsu, E., Narumoto, T., & Totani, T. 2007, MNRAS, 376, 1635
Ando, S., & Pavlidou, V. 2009, MNRAS, 400, 2122
Atwood, W. B., Abdo, A. A., Ackermann, M., et al. 2009, ApJ, 697, 1071
Blake, C., & Wall, J. 2002, MNRAS, 337, 993
Bonoli, S., Marulli, F., Springel, V., et al. 2009, MNRAS, 396, 423
Brookes, M. H., Best, P. N., Peacock, J. A., Röttgering, H. J. A., & Dunlop, J. S. 2008, MNRAS, 385, 1297
Camera, S., Fornasa, M., Fornengo, N., & Regis, M. 2013, ApJL, 771, L5
Camera, S., Fornasa, M., Fornengo, N., & Regis, M. 2014, arXiv:1411.4651
Casandjian, J., & Grenier, I. 2009, arXiv:0912.3478
Casandjian, J. M., et al. 2015, Proceedings of the 5th Fermi Symposium, arXiv:1502.07210
Challinor, A., & Chon, G. 2005, MNRAS, 360, 509
Cholis, I., Hooper, D., & McDermott, S. D. 2014, JCAP, 2, 14
Chon, G., Challinor, A., Prunet, S., Hivon, E., & Szapudi, I. 2004, MNRAS, 350, 914
Condon, J. J., Cotton, W. D., Greisen, E. W., et al. 1998, AJ, 115, 1693
Cooray, A., & Sheth, R. K. 2002, PhR, 372, 1
Cuoco, A., Brandbyge, J., Hannestad, S., Haugboelle, T., & Miele, G. 2008, PhRvD, 77, 123518
Cuoco, A., Komatsu, E., & Siegal-Gaskins, J. M. 2012, Phys. Rev. D, 86, 063004
De Zotti, G., Massardi, M., Negrello, M., & Wall, J. 2010, ARA&A, 18, 1
Dermer, C. D. 2007, ApJ, 659, 958
di Mauro, M., Calore, F., Donato, F., Ajello, M., & Latronico, L. 2014, ApJ, 780, 161
Dobardžić, A., & Prodanović, T. 2014, ApJ, 782, 109
Efstathiou, G. 2004, MNRAS, 348, 885
Efstathiou, G. 2004, MNRAS, 349, 603
Fichtel, C. E., Kniffen, D. A., & Hartman, R. C. 1973, ApJL, 186, L99
Fields, B. D., Pavlidou, V., & Prodanovic, T. 2010, arXiv:1003.3647
Fornengo, N., Perotto, L., Regis, M., & Camera, S. 2014, arXiv:1410.4997
Fornengo, N., & Regis, M. 2014, FrPhy, 2, 6
Giannantonio, T., Crittenden, R., Nichol, R., & Ross, A. J. 2012, MNRAS, 426, 2581
Giannantonio, T., Scranton, R., Crittenden, R. G., et al. 2008, PhRvD, 77, 123520
Górski, K. M., Hivon, E., Banday, A. J., et al. 2005, ApJ, 622, 759
Gruppioni, C., Pozzi, F., Rodighiero, G., & Delvecchio, I. 2013, MNRAS, 432, 23
Hernández-Monteagudo, C., Ross, A. J., Cuesta, A., et al. 2014, MNRAS, 438, 1724
Ho, S., Cuesta, A., Seo, H.-J., et al. 2012, ApJ, 761, 14
Inoue, Y. 2011, ApJ, 733, 66
Inoue, Y., & Totani, T. 2009, ApJ, 702, 523
Inoue, Y., Totani, T., & Mori, M. 2010, PASJ, 62, 1005
Jarrett, T., Chester, T., Cutri, R., et al. 2000, AJ, 120, 298
Keshet, U., Waxman, E., & Loeb, A. 2004, JCAP, 4, 6
Koutoulidis, L., Plionis, M., Georgantopoulos, I., & Fanidakis, N. 2013, MNRAS, 428, 1382
Kraushaar, W. L., Clark, G. W., Garmire, G. P., et al. 1972, ApJ, 177, 341
Landy, S. D., & Szalay, A. S. 1993, ApJ, 412, 64
Laureijs, R., Amiaux, J., Arduini, S., et al. 2011, arXiv:1110.3193
Lewis, A., Challinor, A., & Lasenby, A. 2000, ApJ, 538, 473
Lindsay, S. N., Jarvis, M. J., Santos, M. G., et al. 2014, MNRAS, 440, 1527
Makiya, R., Totani, T., & Kobayashi, M. A. R. 2011, ApJ, 728, 158
Mayer-Hasselwander, H. A., Kanbach, G., Bennett, K., et al. 1982, A&A, 105, 164
Myers, A. D., Brunner, R. J., Richards, G. T., et al. 2006, ApJ, 638, 622
Nolan, P. L., Abdo, A. A., Ackermann, M., et al. 2012, ApJS, 199, 31
Overzier, R. A., Röttgering, H. J. A., Rengelink, R. B., & Wilman, R. J. 2003, A&A, 405, 53
Padovani, P., Ghisellini, G., Fabian, A. C., & Celotti, A. 1993, MNRAS, 260, L21
Persic, M., de Zotti, G., Boldt, E. A., et al. 1989, ApJ, 336, L47
Ade, P. A. R., Aghanim, N., et al. Planck collaboration 2013a, arXiv:1303.5079
Ade, P. A. R., Aghanim, N., et al. Planck collaboration 2013b, arXiv:1303.5075
Rassat, A., Land, K., Lahav, O., & Abdalla, F. B. 2007, MNRAS, 377, 1085
Rephaeli, Y., & Persic, M. 2013, in Advances in Solid State Physics: Cosmic Rays in Star-Forming Environments Vol. 34, ed. D. F. Torres, & O. Reimer (Berlin: Springer), 193
Richards, G. T., Nichol, R. C., Gray, A. G., et al. 2004, ApJS, 155, 257
Richards, G. T., Myers, A. D., Gray, A. G., et al. 2009, ApJS, 180, 67
Rodighiero, G., Vaccari, M., Franceschini, A., et al. 2010, A&A, 515, A8
Rolke, W. A., Lopez, A. M., & Conrad, J. 2005, NucIM, A551, 493
Ross, A. J., Ho, S., Cuesta, A. J., et al. 2011, MNRAS, 417, 1350
Schlegel, D., Abdalla, F., Abraham, T., et al. 2011, arXiv:1106.1706
Schlegel, D. J., Finkbeiner, D. P., & Davis, M. 1998, ApJ, 500, 525
Scranton, R., Johnston, D., Dodelson, S., et al. 2002, ApJ, 579, 48
Shirasaki, M., Horiuchi, S., & Yoshida, N. 2014, PhRvD, 90, 063502
Smith, R. E., Peacock, J. A., Jenkins, A., et al. 2003, MNRAS, 341, 1311
Sreekumar, P., Bertsch, D. L., Dingus, B. L., et al. 1998, ApJ, 494, 523
Stecker, F. W., & Salamon, M. H. 1996, ApJ, 464, 600
Stecker, F. W., & Venters, T. M. 2011, ApJ, 736, 40
Strong, A. W., Moskalenko, I. V., & Reimer, O. 2004, ApJ, 613, 956
Su, M., Slatyer, T. R., & Finkbeiner, D. P. 2010, arXiv:1005.5480
Szapudi, I., Prunet, S., & Colombi, S. 2001, ApJL, 561, L11
Tamborra, I., Ando, S., & Murase, K. 2014, arXiv:1404.1189
Thomas, S. A., Abdalla, F. B., & Lahav, O. 2011, PhRvL, 106, 241301
Willott, C. J., Rawlings, S., Blundell, K. M., Lacy, M., & Eales, S. A. 2001, MNRAS, 322, 536
Wilman, R. J., Miller, L., & Jarvis, M. J. 2008, MNRAS, 388, 1335
Xia, J., Viel, M., Baccigalupi, C., & Matarrese, S. 2009, JCAP, 9, 3
Xia, J.-Q., Cuoco, A., Branchini, E., Fornasa, M., & Viel, M. 2011, MNRAS, 416, 2247
Xia, J.-Q., Viel, M., & Baccigalupi, C. 2010, ApJL, 717, L17